Some Physical Mechanisms for Efficient Swimming

A Dissertation

Presented to

the faculty of the School of Engineering and Applied Science

University of Virginia

---

in partial fulfillment

of the requirements for the degree

Doctor of Philosophy

by

Mehdi Saadat

December

2014

APPROVAL SHEET

The dissertation

is submitted in partial fulfillment of the requirements

for the degree of

Doctor of Philosophy

Mehdi Saadat

AUTHOR

The dissertation has been read and approved by the examining committee:

Hossein Haj-Hariri

Advisor

Alexander Smits

Hilary Bart-Smith

Haibo Dong

Frank Fish

George L. Cahen

Accepted for the School of Engineering and Applied Science:

Dean, School of Engineering and Applied Science

December

2014

Abstract

The central goal of this dissertation is to illustrate some of the fundamental physics of efficient swimming. Specifically, physical explanations are provided for two significant observations:

(a) Fish exhibit a tight range of Strouhal number, $0.2 < St < 0.4$, defined as tail-beat frequency multiplied by wake width divided by swimming speed, ($St = fA/U$), and

(b) Most fish (such as trout, dace, goldfish, cod and dolphins) maintain constant tail-beat amplitude during cruise, and their speed is correlated linearly with their tail-beat frequency.

A computational and theoretical approach is undertaken to study the performance and wake patterns of a two-dimensional model of fish that consists of a virtual body (source of drag) connected to a pitching foil (source of thrust). The model helps elucidate the role of Strouhal number in free swimming in general, and it provides a framework for explaining the reasons behind observations (a) and (b) above.

It is shown that the prevalent interpretation of *St* as a sufficient measure of efficiency is too broad, because Strouhal number is only a function of the shape (i.e. drag coefficient) and area of the body. In fact Strouhal number becomes effectively constant at higher speeds of swimming, and its value does not depend on the gait regardless of the speed. This conclusion follows from showing that the thrust coefficient for the pitching foils of this study is a function of only the Strouhal number for all gaits whose amplitude is less than a certain critical value. The finding is generalized by performing a

dimensional analysis, and it is shown that the variation of Strouhal number with cruising speed is simply related to the variation of the body drag coefficient with speed.

Additionally, for pitching foils, a unique optimum point is identified in the dimensionless frequency vs. amplitude plane, where power efficiency is maximized. It is hypothesized that the better swimmers in nature are those whose body drag is matched perfectly to the thrust of their propulsor at the point of maximum efficiency of the propulsor. When so matched, the resulting swimmer will remain at its optimum power point and swim efficiently at all other speeds as well, so long as the swimmer controls its speed by maintaining fixed flap amplitude and modulating the frequency of the flap.

A final goal of this work is to investigate some aspects of the hydrodynamics of batoids utilizing pectoral-fin-based propulsion. A computational study is conducted to investigate the effect of wing planform and kinematics on the performance of a three-dimensional batoid fin. Full fluid-structure interaction analysis, as well as prescribed kinematics approaches are utilized. The computational results are validated against experimental measurements.

Acknowledgements

I have had an amazing journey during my tenure as a PhD student that allowed me to mature both scientifically and personally. Graduate school has been a great opportunity to extensively improve my thought process, my eagerness to understand the world around me and make great friendships. I would like to thank my advisor, Hossein Haj-Hariri, for the privilege of working with him during my PhD studies. His knowledge and understating of scientific problems as a whole and fluid mechanics and heat transfer in part, was the main courage that let me to take on this journey and learn from him.

I have been grateful to have the opportunity to be a part of an amazing team to tackle some of the most complex problems in nature. I would like to thank the PI, co-PIs and program manager of the MURI team, Hilary Barth-Smith, Robert Brizzolara, Hossein Haj-Hariri, Lex Smits, Frank Fish, Silvia Blemker, and Ted Iwasaki for their great discussions and brainstorming that allowed me to think better about the problems and come up with better solutions. I would also like to thank Harsha Chelliah for the support and opportunities during the past year.

I would like to thank my fellow teammates Keith Moored, Dan Quinn, Peter Dewey, Jean-Noel Pederzani, Trevor Kemp, Scott Russo, Joe Zhu and Zheng Chen for all the in-depth and fun discussions about fish swimming. I would like to thank my fellow office mates Reza Monazami and Sae-Woong Kil for few years of professional and fun conversations. At the end, I would like to emphasize that without the support of my family, this journey would have been far from complete. It is the unconditional love that I have received from them throughout my entire life that allowed me being where I am

today. I will continue my journey through the river of success to make my family and friends happy.

This work was supported mainly by the Office of Naval Research MURI grant number N00014-08-1-0642, under Program Director Dr. Bob Brizzolara. Further support was provided by Farrar and Sidebottom Fellowships from the University of Virginia. The above financial support is hereby gratefully acknowledged.

Contents

List of Figures

List of Tables

Nomenclature

A	Flapping amplitude
AR	Wing aspect ratio
A^*	Non-dimensional amplitude
$A^*_{critical}$	Critical amplitude
A^*_{opt}	Non-dimensional amplitude of the maximum-efficiency point
b	Span length
$\mathbf{b}$	External forcing
c	Chord length
C_D	Body drag coefficient
C_d	Section drag coefficient
C_l	Section lift coefficient
C_P	Power coefficient
$C_{pressure}$	Pressure coefficient
C_Q	Constant
C_T	Thrust coefficient
$\widetilde{C_T}$	New thrust coefficient
$\mathrm{C}(k)$	Theodorsen's function
D	Drag
d_N	Normal distance from the surface

E	Modulus of elasticity
f	Flapping frequency
$\mathbf{f}$	Acceleration of the external body force
$\boldsymbol{F}$	Fluid force at the surface
f^*	Non-dimensional frequency
f^*_{opt}	Non-dimensional frequency of the maximum-efficiency point
k	Reduced frequency
K	Fitting parameter
K_s	Mean strain rate
L	Total lift
ℓ	Length scale
ℓ_D	Body length
ℓ_T	Propulsor length
L_1	Circulatory lift
L_2	Non-circulatory lift
m	Fitting parameter
M_0	Instantaneous moment
n	Fitting parameter
P	Transient power deposited to the fluid
$\bar{P}$	Cycle-averaged power
p	Pressure field
Q	Q-criterion
$\boldsymbol{r}$	Distance from upwind point to integration point (in a mesh element)

Re	Reynolds number
Re_D	Body-based Reynolds number
S	Planform area
S_D	Wetted area of the body
S_T	Planform area of the propulsor
St	Strouhal number
t	Time
T	Transient thrust
$\bar{T}$	Cycle-averaged thrust
TR	Wing taper ratio
t_P	Cycle period
$\boldsymbol{u}$	Velocity field
U	Forward swimming or flying speed
$\boldsymbol{U_{eff}}$	Effective velocity
U_1	Speed corresponding to minimum power
U_2	Speed corresponding to maximum range
$\boldsymbol{V}$	Surface velocity
x	Eulerian coordinate in the direction of motion
$\mathbf{x}$	Time-dependent position
$\mathbf{X}$	Initial position
x_f	Lagrangian x coordinate
y	Eulerian coordinate normal to the direction of motion
Y	Heave amplitude

Y_{max}	Maximum heave amplitude
y_f	Lagrangian y coordinate
y^+	Non-dimensional distance from the surface
z	Eulerian coordinate bi-normal to the direction of motion
α	Pitch angle
α_{eff}	Effective angle of attack
α_{max}	Maximum pitch angle
β	Scheme indicator
Γ_{disp}	Mesh stiffness
δ	Relative mesh displacement
ε	Constant to avoid singularity of Γ_{disp}
η	Froude efficiency
μ	Dynamic viscosity
ν	Kinematic viscosity, and also Poisson's ratio
ρ	Fluid density
ρ_S	Solid density
σ	Cauchy stress tensor
ϕ	Solution value
ϕ_{ip}	Solution value at the integration point
ϕ_{up}	Solution value at the upwind point
Ω	Vorticity Magnitude
ω	Angular frequency

Chapter 1

Motivations and Objectives

While most Autonomous Underwater Vehicles (AUVs) are capable of performing complex missions, their performance remains limited when compared with solutions from nature. For instance, screw propellers [1] have a narrow window of efficiency, are noisy, and also lead to vibrations [2]. AUVs also have low maneuverability (e.g. large turning radius), and limited supply of power. These limitations continue to drive engineers to envision and design unconventional underwater propulsion platforms to overcome the current limits on efficiency and performance.

Nature, through the benefit of evolution, is a great source of inspiration for the design of novel underwater propulsors. Propulsion in the form of flapping in which the animal imparts momentum into the fluid by flapping its pectoral or caudal fin [3] is the most common within the swimming species. There have been several efforts in designing and building bio-mimetic swimming robots. Examples are based on tuna ([4], [5], [6]), lamprey ([7], [8]), and dolphin [9]. Overall, flapping-based propulsion platforms are still far from mainstream, mainly due to a lack of detailed understanding of the underlying fluid physics underlying efficient self propulsion.

Fish locomotion can generally be classified into two different categories: fish that swim by passing a traveling wave down the body and caudal fin (body/caudal fin

propulsion) or the ones that use a combination of pectoral, dorsal and anal fins for propulsion (median/paired fin propulsion). In either case, fish swimming gait lies on a spectrum between the two extremes of undulatory and oscillatory movements [10], [11], [12]. In the undulatory case, the fish uses its entire body to generate propulsive force whereas in the oscillatory movement, the fish incorporates part of its body for thrust generation and the other part is mainly associated with drag. Figure 1.1 summarizes different forms of swimming gaits (adopted from [11]).

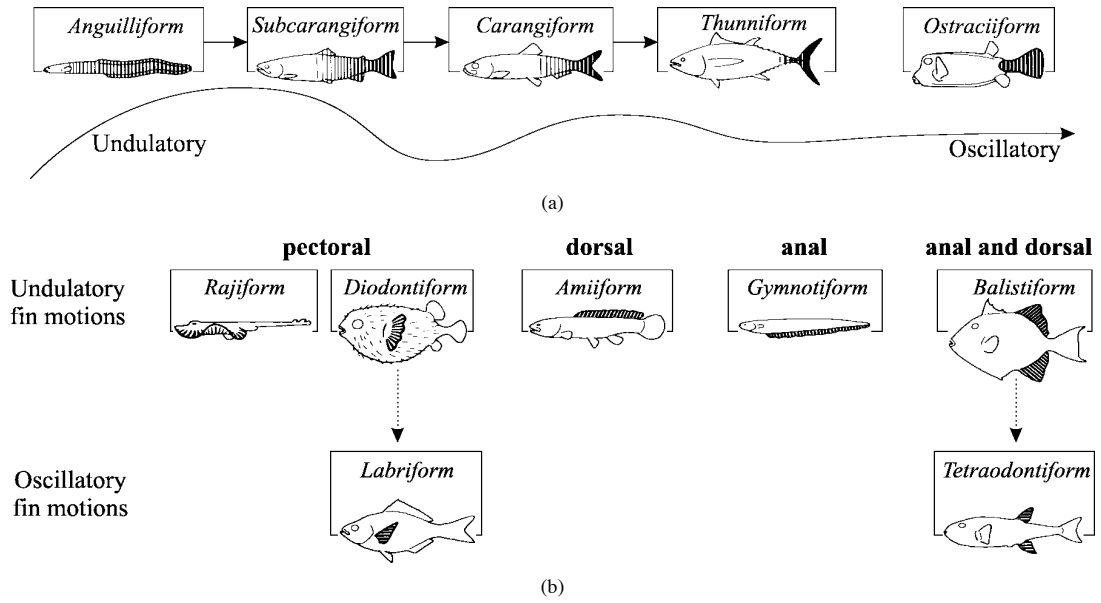

Figure 1.1: Comparison of different swimming gaits for Body/caudal fin and Median/paired fin type of locomotion. Adopted from [11].

Among the swimming species that utilize oscillatory flapping propulsion (in median/paired fin category) is the manta ray (Manta birostris) (Fig. 1.2c), a particular species of Batoidea (rays). Manta rays are characterized by the large deformations of their giant dorsoventrally flattened pectoral fins [13], which allows them to achieve high levels of agility in maneuvering and prey catching, as well as high propulsive efficiency

([14] and [15]). Little is known about how they utilize their fin flexibility to attain these superior performances. In particular, it is unknown to what extend the animal controls its fin deformation (active flexibility) and to what extend the fin deformation is the outcome of the interaction of the flexible fin with the fluid forces (passive flexibility). Additionally, the role of spanwise and chordwise flexibility in the overall performance of the fin remains an unresolved issue (see [16] and [17] for the discussions on the relation of flexibility and efficiency for pectoral fins). Given that manta rays achieve superior swimming performance by using a unified mechanical system for both propulsion and control (i.e. their pectoral fin), they remain an interesting complex biological model for scientists to study. According to [2], manta rays outperform the current AUV technology in the following areas:

1 – Lower noise generation

2 – Maneuverability

3 – Station keeping ability

4 – Burst swimming speed

5 – Efficiency (or economy)

Table 1.1 contrasts the performance data for manta rays and AUVs on the market today.

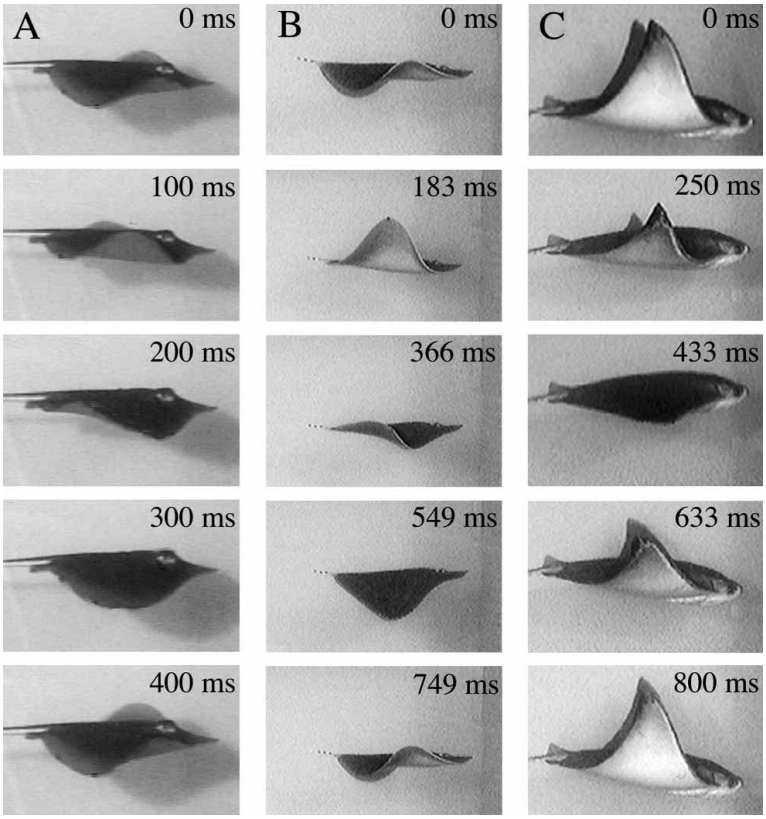

Figure 1.2: Snapshots of three species of ray family swimming at 2 body length per second at different times during the flapping cycle. The rays are classified based on swimming gait for (A) undulatory (B) intermediate (undulatory-oscillatory) (C) oscillatory locomotion. Adopted from [13].

Performance Metrics	Glider	MBARI	Work Class	Manta Ray
Speed (BL/s)	0.22	0.25	0.25	1-2
Length (m)	1.8	6	6.1	1.8
Range (km)	1500	50	1.2	640
Turn Radius (BL)	4	1.7	0	0.5
Turn Rate (rad/s)	0.055	0.15	N/A	3.15
Economy (BL/kJ)	100	0.36	N/A	3

Table 1.1: Comparison of performance for manta rays with that of current AUV technology. Adopted from [18].

Designing an efficient underwater biomimetic robot is an iterative multidisciplinary collaboration among hydrodynamics, control engineering, structural design, and biology. The starting point in this iteration is to observe and quantify the kinematics of the animal. The resulting data is then used to analyze and develop the corresponding computational and experimental models. Common kinematic behaviors among swimming species are of great interest since they often (but not necessarily) correspond to a certain cost function that is being optimized by the animal for a specific purpose. Fish schooling and burst-and-coast swimming are two examples of such common behaviors that have been correlated to mechanical power minimization by fish ([19] and [20]). Understanding the underlying energetic principles behind these kinematic observations has profound implications for design and developing highly efficient underwater robots.

Taylor [21] suggested that although swimming (and flying) species differ in morphology and flapping mechanisms when cruising, they yet share a common aspect of locomotion characterized by a narrow range of Strouhal number, $St = fA/U$, where U is the swimming speed, f is the frequency of flapping and A is the width of the wake behind the flapping appendage, and is usually assumed to be tip-to-tip excursion of the trailing edge (Fig. 1.3). Moored et al. [22] conducted an experiment using an elliptical undulating wing that was set to swim freely, and showed that the St corresponding to cruise for all the considered wavelengths converged to a tight range of 0.2-0.4 similar to that observed for manta rays (Fig. 1.3), thereby augmenting the observations of [21] to include ray species.

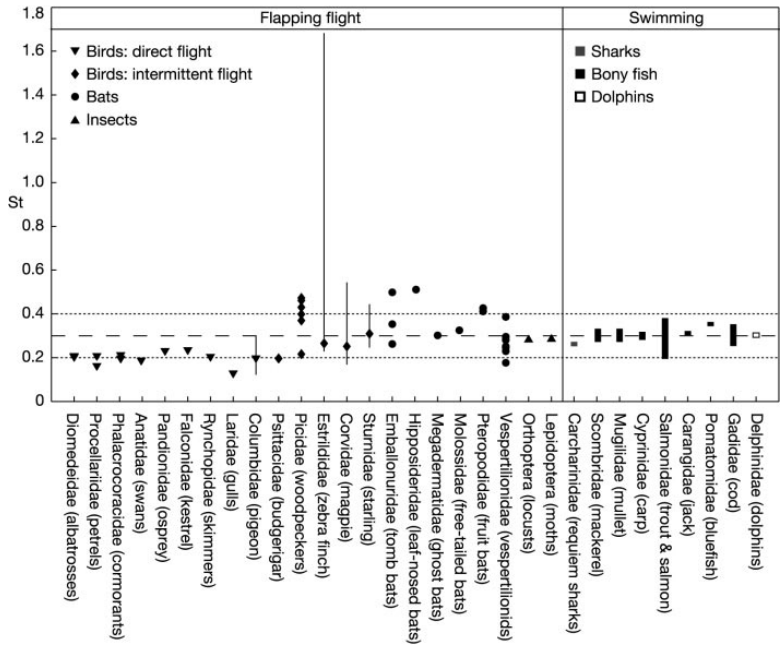

Figure 1.3. The observed cruising Strouhal number for various flying and swimming animals. The tight range of St corresponding to the swimming animals (0.2-0.4) is the focus of this study. Adopted from [21].

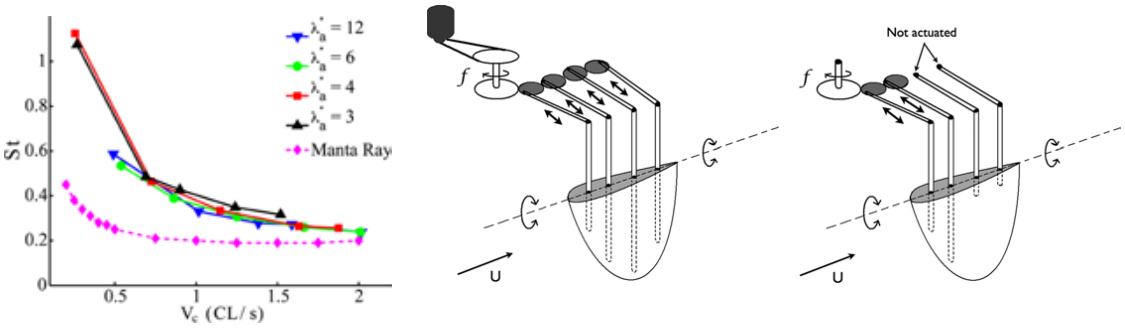

(a) (b)

Figure 1.4: Strouhal number as a function of swimming speed (cruise condition) for an experimental fin compared with biological data for manta ray. (b) the experimental fin used to calculate the Strouhal number for different wave number at (a). Adopted from [22].

In addition to the tight range of St, it has been observed that fish and cetaceans (for instance trout, dace, goldfish and dolphin) gain or reduce cruising speed mainly by altering the frequency of their tail beat while maintaining the tail-beat amplitude at a fairly constant level [23-24]. The same behavior has also been reported for cownose rays [25]. Figures 1.5-1.7 plot the variation of tail-beat frequency and amplitude as a function of swimming speed for various fish and cetaceans species. Considering the morphological difference between cetaceans and ray species, these common kinematic behaviors seem to be pointing to a fundamental principle that holds in free-swimming.

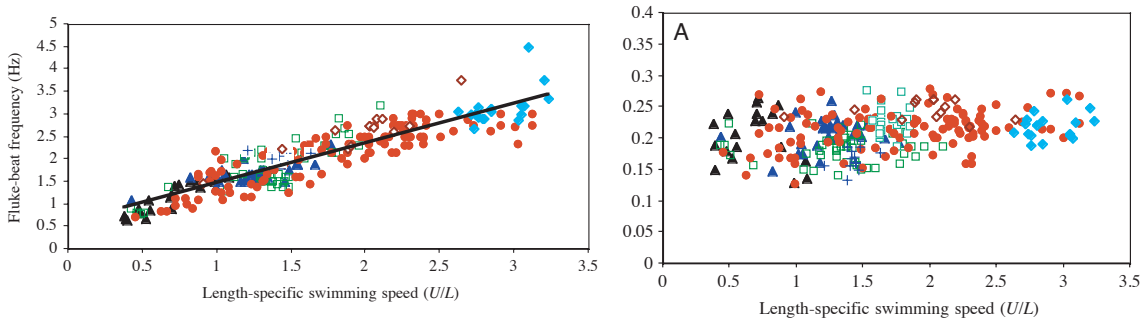

(a) (b)

Figure 1.5. Variation of tail-beat (a) frequency and (b) amplitude with respect to cruising speed for 248 captive odontocete cetaceans. Adopted from [24].

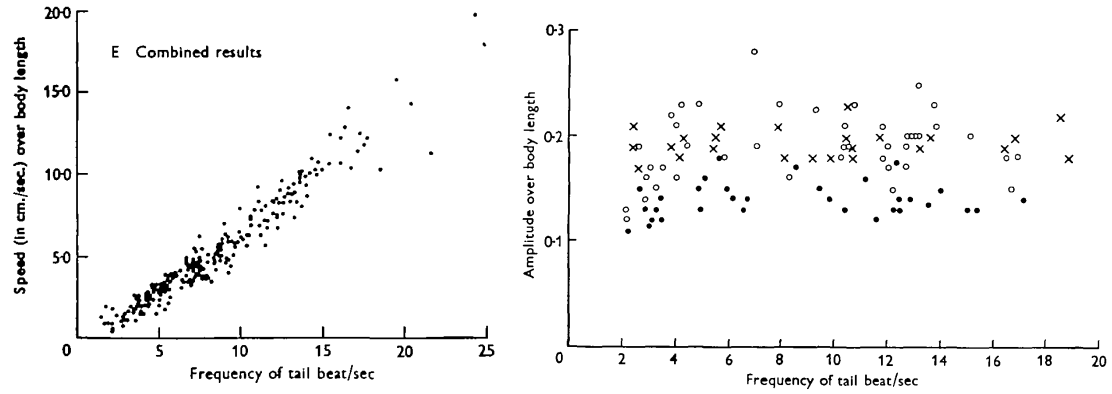

(a) (b)

Figure 1.6. Variation of (a) tail-beat frequency with respect to swimming speed and (b) amplitude with respect to flapping frequency for captive dace, trout and goldfish. Note since frequency is linearly correlated with speed, swimming speed and frequency can interchangeably be used on the horizontal axis of (b). Adopted from [23].

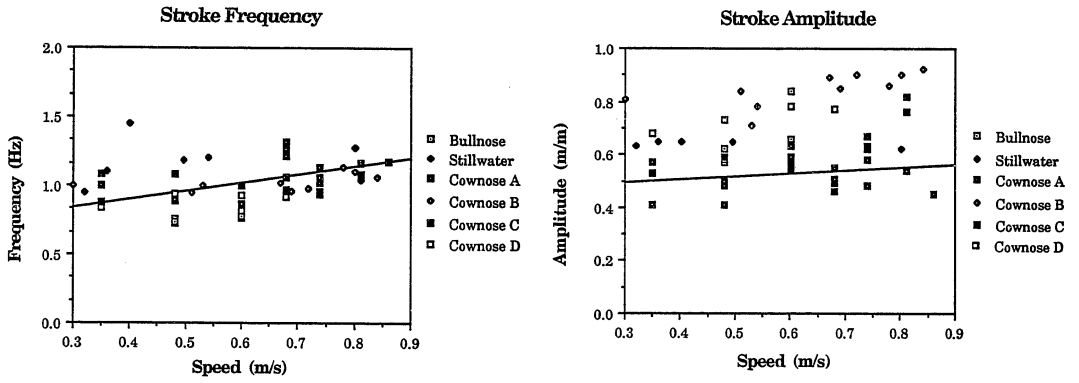

(a) (b)

Figure 1.7. Variation of tail-beat (a) frequency and (b) amplitude with respect to swimming speed for cownose ray. Adopted from [25].

One goal of this work is to understand the fundamentals behind ray swimming. The focus will be on the performance rather than the structure of the wake, but wake visualization will be performed also. To do so, first, a three-dimensional model of batoid wing is developed, replicating the experimental prototype built by Moored [18]. The computational results are validated against experimental data. Then, a parametric study is performed to investigate the effects of kinematics on the performance of the wing. Both fluid-structure interaction and prescribed-motion analyses are considered in this work. However, the ***main goal of this research is to provide physical explanations for the aforementioned common kinematics behaviors among swimming species (i.e. the tight range of Strouhal number as well as the maintenance of the flapping amplitude at cruise) through a computational and theoretical study.*** To achieve this goal, the following questions need to be addressed:

1 – How does Strouhal number, St, vary in free-swimming?

2 – How is propulsive efficiency (defined as $\eta = \bar{T}U_\infty/\bar{P}$, where U_∞ is free stream velocity, $\bar{T}$ is cycle-averaged net streamwise force herein termed thrust, and $\bar{P}$ is the cycle-averaged power inserted to the flow) interpreted in free-swimming, where the net force is zero?

3 – How do energy considerations lead to optimal gait or swimming speed?

4 – What are the necessary and sufficient conditions for (energetically) efficient swimming?

To answer the questions above, a simple two-dimensional model of a fish that consists of a generic body, as the source of drag, and a propulsor, as the source of thrust, is adopted. This model is intended to approximate the locomotion of thunniform vertebrates (cetaceans, tunas, sharks). Note that for the forms of fish locomotion on the far left side of undulatory-oscillatory spectrum (Fig. 1.1), thrust and drag cannot be distinguished, and the present model is only of qualitative value. A comprehensive set of numerical experiments (performed using the commercial Computational Fluid Dynamics (CFD) package ANSYS® CFX, release 14.0) in conjunction with theoretical modeling is conducted to study the hydrodynamics of pitching foils within the context of free-swimming. The two-dimensional computational results are validated against the experimental data obtained by Dewey [90].

The remainder of this dissertation is organized as follow: chapter 2 provides a literature review for flapping propulsion. In particular, it highlights the unresolved issues for fish swimming within the context of free-swimming. In Chapter 3, a three-dimensional batoid flapping wing model is developed based on the experimental

prototype built by Moored [18], with the intention of replicating the geometry and dynamic deformation of manta ray pectoral fin. Effects of planform taper ratio and other kinematic parameters on the performance and wake dynamics of the fin are studied by undertaking two approaches for the wing deformation: (a) fully-coupled fluid-structure interaction analysis, where the wing is modeled as a flexible skin that deforms by the oscillatory movement of a rigid inner structure, and its passive deformation is calculated by solving the coupled fluid and solid solvers and (b) prescribed motion, where the deformation of the wing surface is prescribed according to the mathematical model in [18], and replicates the movement of the manta ray fin. Chapter 4 introduces a simple fish model that consists of a generic body and a two-dimensional pitching foil to expand upon the findings of the earlier chapters and to provide physical explanation for the tight range of *St*, and for the constancy of the amplitude of the flapping among swimming species. The computational results are further supported by analytical solutions. Dimensional and scaling analyses are then utilized to generalize the findings further. Chapter 5 elucidates the numerical methodology that is used in the commercial software ANSYS CFX. Mesh study and code validation are further presented in this chapter. Chapter 6 concludes the findings of this dissertation and provides a roadmap for future work.

Chapter 2

Background on flapping propulsion

Knoller [26] and Betz [27] theorized that heaving airfoils could generate thrust in a uniform stream. They attributed the generated thrust to the effective angle of attack of the incoming flow, which causes the normal force to have a component in the streamwise direction (Fig. 2.1). Katzmayr [28] provided experimental verification of this finding and further noted the reduction of drag, now known as Katzmayr effect. Ober [29] offered a simple explanation of the cause of the Katzmayr effect.

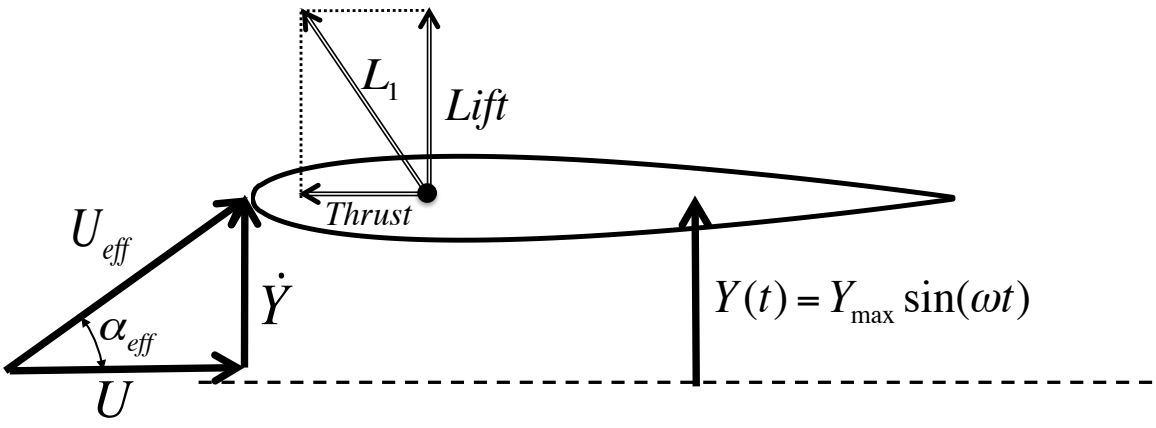

Figure 2.1: A schematic illustration of how thrust is generated by altering the effective angle of attack seen by an airfoil. Note that total circulatory force $\boldsymbol{L_1}$ is perpendicular to effective velocity $\boldsymbol{U_{eff}}$.

The equations of ideal flow provided the first mathematical tool for explaining the mechanism of thrust generation by an airfoil undergoing small-amplitude heaving oscillations [30-32]. The linearized formulations predicted that all heaving motions generate thrust by shedding a vortex wake behind the airfoil. Moreover, it was noted that Froude efficiency increased monotonically as the frequency of flapping approached zero. Wang [33], among others, noted the paradoxical nature of the conclusion: a flying or swimming animal should flap at frequencies very close to zero to achieve the best propulsive efficiency. Even after extending the inviscid theory to include nonlinearities and large amplitude motions, Lighthill [34], Chopra and Kambe [35], Chopra et al. [36], Wu [37] and Phlips et al. [38] predicted the same monotonic dependence of efficiency on flapping frequency, i.e. that the efficiency is maximized as frequency goes to zero. This paradox is resolved upon introduction of viscous effects, as outlines later in the chapter.

There have been efforts to extend the Prandtl lifting-line theory to unsteady flows. Ahmadi and Widnall [39] calculated the propulsive forces and energetics of an oscillating wing with finite span (for small amplitudes) using the linearized unsteady wing theory. Willmott [40] extended the method developed by Ahmadi and Widnall [39] using matched asymptotic expansions to investigate the forces acting on high-aspect ratio wings. The primary outcome of the model developed by [40] is an expression for downwash due to three-dimensional effects. Betteridge and Archer [41] and Archer et al. [42] introduced a method that included twisting of the wing but ignored the unsteady effects of the wake. Phlips et al. [38] improved the approach by modeling the unsteady wake using a vortex sheet as well as discrete vortices. However, the models were not able to account for the self-induced convection of the wake. It should be noted that lifting-line

methods are based on linearized equations and are not able to predict accurate results for high amplitude oscillations.

As another extension from Prandtl lifting-line theory, Vortex Lattice Method was used by Hall and Hall [43] to examine the optimal circulation distribution of a flapping wing that is simultaneously generating thrust and lift in forward flight. Using the Betz criterion for optimal propellers, they determined the time-dependent optimal circulation along the span, which translates into the optimal wake configuration that minimizes the induced power loss. Hall et al. [44] added a viscous drag component to the method developed by Hall and Hall [43]. Using a variational principle that was essentially the viscous extension of Betz criterion, the necessary condition for the optimal circulation distribution was found.

Another commonly used modeling tool in aerodynamics is the panel method. Modern variations of traditional Panel methods provide fast computational tools to analyze flows induced by flapping. Katz and Plotkin [45] developed a panel method, which was later used by Smith et al. [46] to model the flight of a tethered sphenoid moth. The apparent deviation of the horizontal force calculated by their code from experimental results can be attributed to inability of inviscid methods to predict leading edge separation [47]. Jones et al. [48] developed a panel code to investigate the propulsive forces and hydrodynamic efficiency of a two-dimensional airfoil undergoing heaving and pitching motion. Additionally, a boundary layer correction was devised to estimate the viscous drag of the airfoil. Detailed comparison of the results with experiments showed the evolution of the wake behind a flapping airfoil to be essentially an inviscid phenomenon. It was also observed that for Strouhal numbers greater than unity, the wake

loses its symmetry and deflects from the centerline. Also the hydrodynamic efficiency exhibited a monotonic decrease with Strouhal number, so that maximum efficiency occurred as frequency approached zero.

Strouhal number has been considered as a dimensionless parameter with significant importance for studying flapping propulsion. *St* was initially introduced by Triantafyllou et al. [49] as a wake-based scaling parameter, which before then had been used to describe the wake behind stationary flow obstructions [50]. Since then, a vast body of literature has been devoted to characterizing the performance of oscillating foils with regard to *St*. For instance, Anderson et al. [51], Lewin and Haj-Hariri [47], Clark and Smits [16], Buchholz and Smits [52] and Godoy-Diana et al. [53] have shown that the streamwise force generated by the oscillating foils, has a threshold of thrust corresponding to some Strouhal number above which thrust is generated, and beyond the threshold, thrust increases with *St*. In an experimental study, Lai et al. [54] designated $St \approx 0.06$ as the threshold of thrust in the drag-thrust spectrum for a purely heaving foil. They concluded foils that do not oscillate fast enough ($St \lesssim 0.06$), do not inject sufficient momentum into the flow to overcome the net drag. More recently, Schnipper et al. [55] and Godoy-Diana et al. [53] performed experiments to identify the vortex structures in the wake of a pitching foil. The results were presented in a phase diagram displaying vortex wakes as a function of frequency and amplitude. They showed that the transition between the von Karman wake - drag indicator - and the inverted von Karman wake - thrust indicator - occurs at $St = 0.18$.

Contrary to the results obtained using inviscid models for flapping foils, in viscous flow, Froude efficiency peaks over the spectrum of St somewhere in between the thrust threshold and infinity. For instance, Triantafyllou et al. [49] and Anderson et al. [51] conducted an experiment in which they isolated a two-dimensional oscillating foil and placed the model in a constant stream to measure the force and power produced by the foil. They confirmed the existence of a peak for propulsive efficiency when plotted against *St*. Further, by comparing the Froude efficiency for different modes of swimming (i.e. different combinations of frequency and amplitude), they showed that maximum propulsive efficiency falls within a narrow range of Strouhal numbers ($0.2 < St < 0.4$), even though for half of the considered motions, the corresponding *St* fell outside of the reported range. They hypothesized that the observed tight range of *St* among swimming species is an indication of the hydrodynamic efficiency of the animal's tail. Anderson et al. [51] further attributed the peak in efficiency to the amalgamation of trailing edge vortices with the shed leading edge vortices. It was suggested that the phase difference between the heave and the pitch motion plays a critical role in determining the value of maximum efficiency since it controls the timing for shedding of the leading edge vortices.

Similar results were obtained in three-dimensions by Clark and Smits [16], Buchholz and Smits [52] and Dong et al. [56] however with lower value for maximum efficiency than that for the two-dimensional foil. Also in some cases, for instance as reported by Dong et al. [56], the *St* corresponding to maximum efficiency ($0.5 < St < 0.9$) fell outside of the range observed in nature. Although all the aforementioned experiments confirmed the existence of maxima in propulsive efficiency for flapping

foils, the predicted values for the corresponding St had great variability among different experiments, and showed sensitive dependence on the details of the flapping motion, incoming flow speed and the shape of the foil cross-section.

Wang [33] conducted a numerical study to investigate the unsteady forces acting on impulsively started airfoils for a fixed incoming flow speed, and various angles of attack. She suggested that the optimum frequency for a given Strouhal number relies upon two time scales, one for the growth of the trailing-edge vortex, and the other for the shedding of the leading-edge vortex. Using these two time scales, a "thrust window" was defined in which the leading edge vortex stayed attached just enough to generate thrust. She further correlated the preferred *St* with the angle of attack at dynamic stall for a given Reynolds number. In agreement with Wang [33], Lewin and Haj-Hariri [47] confirmed that timing of the leading edge separation is essential for propulsive efficiency in heaving airfoils. They noted that efficiency peaks when leading edge vortex remains attached for the duration of each stroke. They moreover showed that wake patterns behind an oscillating airfoil depend primarily on the evolution of the leading edge vortex: whether it is shed, and how it interacts with trailing edge vortex. It was observed that two vortices shed into the wake per flap when leading edge vortex merged with, and reinforced, the trailing edge vortex, and four vortices shed when the leading edge vortex paired up with the trailing edge vortex. In agreement with Anderson et al. [51], high propulsive efficiencies were obtained when leading edge vortex positively reinforced the trailing edge vortex. Negative reinforcement on the other hand, greatly reduced the measured thrust and efficiency of the motion.

Reynolds number, $Re = \rho U \ell / \mu$ where ρ and μ are the fluid density and dynamic viscosity, on the other hand is the prominent parameter characterizing the effects of viscosity in flapping propulsion. In particular, flow separation (or dynamic stall) is found to be highly dependent on Reynolds number. In fact, leading edge vortices that are byproducts of dynamic stall create low-pressure regions just above the leading edge of the wing [57] and thus play a major role in lift and thrust enhancement of flying insects [58-60]. As has been argued by Lewin and Haj-Hariri [47] and Buchholz and Smits [52] among many others, the effects of unsteadiness (characterized by *St*) dominate the force production of flapping wings as Reynolds number increases.

The signature of the wake created behind the flapping foil is indicative of the ability of the foil to generate thrust. Particularly, the sense of rotation of vortices determines the existence of momentum deficit or jet flow in the wake behind the airfoil [47]. In the case of not enough streamwise momentum to overcome the drag, the well-known Karman vortex street appears in the wake. The vortex street generated behind a stationary cylinder is a good example of drag-based wakes. Conversely, in the case of net thrust, the sense of rotation of the vortices is inverted compared to Karman Vortex Street [e.g. Fig. 2.2].

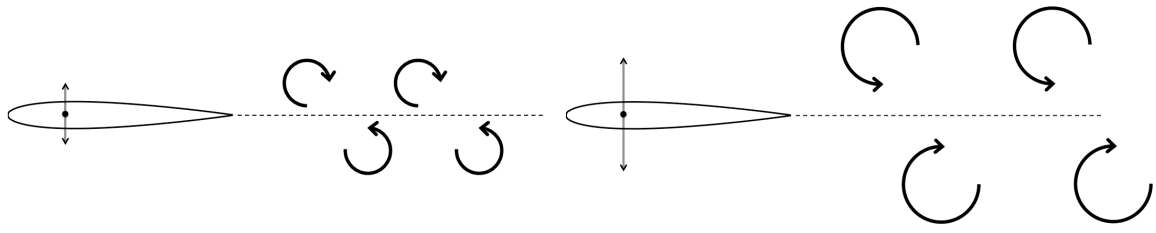

(a) (b)

Figure 2.2: Representative wake behind an oscillating foil when the generated axial force is (a) drag and (b) thrust. The number of vortices can vary.

Koochesfahani [61], Lai et al. [54], and Lewin and Haj-Hariri [47] further emphasized the dependence of wake structure behind the two-dimensional flapping foils on Strouhal number. They showed that for high enough *St*, the wake undergoes a deflection to one side of the symmetry line. More recently, Schnipper et al. [55] and Godoy-Diana et al. [53] performed experiments to identify the vortex structures in the wake of a pitching foil. By plotting the results in a dimensionless frequency versus amplitude space, they reported that the wake transition from von Karman to inverted von Karman wake occurs at $St \approx 0.18$. However, Godoy-Diana et al. [53] found the transition from drag to thrust to occur at slightly higher *St* than the one corresponding to the switching of the pattern in the trailing vortex array. In a similar experiment using pitching foil, Bohl and Koochesfahani [62] noted the dependence of the transverse alignment of the vortices on reduced frequency (defined as $k = 2\pi fc/U$) for some fixed flapping amplitude. In agreement with Godoy-Diana et al. [53], they reported that drag-to-thrust transition does not coincide with the switch in the sense of rotation of the vortices.

There is considerable literature pointing to the wake evolution behind the three-dimensional flapping foils. However, owing to the complexity of the wake patterns, few have reported a concrete conclusion regarding the relation between these wake patterns and *St*. Von Ellenrieder et al. [63], Bolndeaux et al. 64], Dong et al. [56], Clark and Smits [16], Buchholz and Smits [52] and Dewey et al. [65] observed that the wake behind a finite aspect ratio flapping wing consists of horseshoe vortices of alternating sign that are fed from both the leading edge and the trailing edge. More specifically, in an experiment using a rigid rectangular pitching panel, Buchholz and Smits [52] observed two distinct three-dimensional wake patterns with regard to *St*. For small Strouhal numbers,

$0.2 < St < 0.25$, two horseshoe vortices were shed per pitching cycle (known an 2-S according to the terminology of Williamson and Roshko [66]) which when viewed on a spanwise plane, they appeared as inverted von-Karman vortex street. For higher Strouhal numbers $St > 0.25$, two pairs of oppositely signed vortices (2-P) shed per pitching cycle. Additionally, wake bifurcation was observed at $St > 0.25$ where cycle-averaged streamwise velocity field behind the pitching panel showed two oblique jets with an angle with respect to streamwise direction. In another experimental study using an undulating flexible fin to mimic ray locomotion, Dewey et al. [65] found that the three-dimensional wake structure behind the fin was a strong function of both wavelength and *St*. They further categorized the three-dimensional wake pattern into four different structures namely von Karman vortex street, 2P, 2S and bifurcating wake, with the selection being decided by the values of wavelength and *St*. Here, we show that for a given swimmer that is cruising while maintaining a constant flapping amplitude, the wake structure remains invariant and is independent of the speed or the frequency.

According to Dewey et al. [65], a fundamental difference between two-dimensional and three-dimensional wake structures arises from the bifurcating wake, which occurs at Strouhal numbers corresponding to high net thrust generation: In two-dimensions, the bifurcating wake is deflected in one direction as observed by Lewin and Haj-Hariri [47] and Godoy-Diana et al. [53] whereas in three-dimensions, the wake splits into two symmetric jets at an angle to the line of symmetry. It should be noted that bifurcating wakes could potentially give rise to control and stability problems in swimming machines since an additional component of lift is generated as a result of deflected jet.

Wake bifurcation phenomenon can be explained using wake resonance theory. In a recent study, Moored et al. [67] used a linear spatial stability analysis to obtain the most unstable frequency of the time-averaged jet behind a three-dimensional flexible elliptical fin using the data provided by Clark and Smits [16] for a fixed incoming flow speed. By extending the work of Triantafyllou et al. [68] and Lewin and Haj-Hariri [47], they showed that when the driving frequency of the fin was tuned to the most unstable frequency of the jet (termed wake resonance), wake transition occurred and a peak appeared in Froude efficiency. It was further showed that there could be multiple wake resonant frequencies corresponding to multiple peaks in efficiency and multiple wake transitions.

Estimating mechanical power requirements for flapping propulsion is a topic of significant interest and has been addressed by a number of researchers including Pennycuick [69], Rayner [70], Schultz and Webb [71], Spedding [72], Hall and Hall [43], Hall et al. [44]. In the case of flying birds, three-dimensional lifting surfaces suffer an additional contribution to drag because of the downwash resulting form the generation of lift, and the tilting back of the oncoming ‘wind’. This induced drag decreases quadratically with respect to the free stream speed, as opposed to the parasitic drag that increases as a quadratic function of speed. Therefore the required power to overcome both parasite and induced drag will assume a U shape in which the point of minimum power defines a characteristic speed corresponding to minimum mechanical work required per unit time, i.e. maximum endurance. On the other hand, the speed at which the power divided by speed assumes its minimum value is correlated with the minimum

mechanical work per unit distance, i.e. maximum range. Fig. 2.3 shows a typical power-velocity curve for a flying bird adopted from Rayner [70].

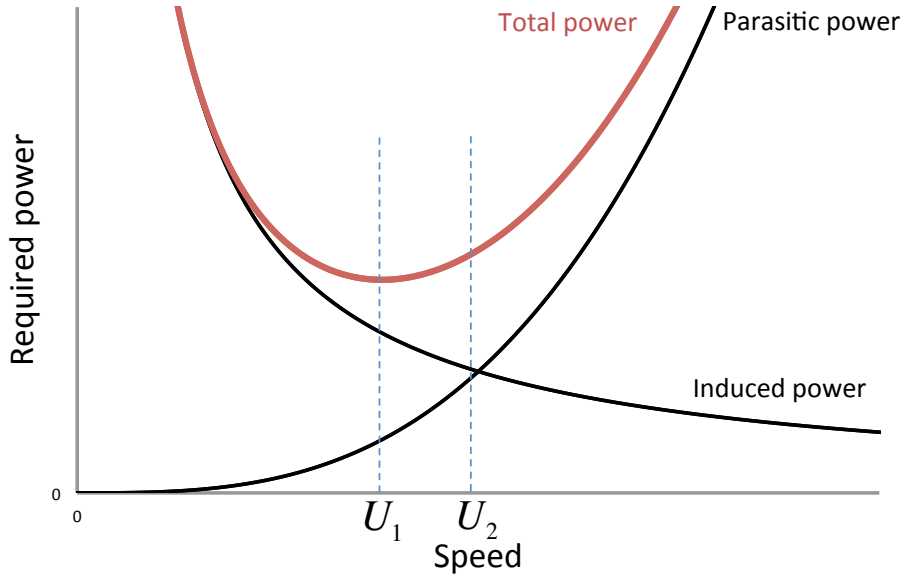

Figure 2.3: A typical power curve for flying crafts/birds. Parasitic power varies as U^3, and induced power varies as U^{-1}. U_1 is the speed for minimum power, and U_2 is the speed for maximum range.

Swimming animals are nearly neutrally buoyant. The force generated by their propulsors contributes mainly to the thrust, and not to any meaningful lift. Therefore, in the case of swimming animals, it is yet unknown if there is any optimum speed at which the mechanical consumed power is minimized. This issue is addressed in this work.

On the relation of Strouhal number to free-swimming, Borazjani and Sotiropoulos [73] conducted a numerical investigation to study the hydrodynamics of carangiform locomotion for various fixed-incoming flow speeds. For each flow speed, they showed there existed a unique *St* at which the total streamwise force on the model returned zero. In agreement with the observations of Lauder and Tytell [3] for Pacific salmon (Oncorhynchus) swimming, Borazjani and Sotiropoulos [73] observed that the *St*

corresponding to cruise was a decreasing function of flow speed, although they did not determine the functional form of this dependence. They further suggested that fish might not be choosing the Strouhal number at which they swim solely based on efficiency considerations, but also with regard to free-swimming.

Webb [74] reviewed the observation in fish locomotion reported by Bainbridge [23] that fish control their swimming speed mostly using tail-beat frequency (such that frequency and speed are linearly correlated) while keeping the amplitude constant, and noted that the principal mechanism behind this observation remains unknown. Webb [74] further raised the question as to why this observation does not seem to hold true when fish swim at speeds close to zero. The answer to this question is also provided in the present dissertation.

Chapter 3

Three-Dimensional Propulsor

Rays with pectoral-fin-based propulsion including manta rays (Manta birostris) and cownose rays (Rhinoptera bonasus), are considered to be highly efficient swimmers [34, 25]. They exhibit high endurance and maneuverability with seemingly little effort [1]. Rays swim using their long flattened pectoral fins, which gives them the ability to acquire large flapping amplitude [13, 25]. One difference between pectoral fin movement of ray species with that of other swimming and flying animals is the lack of a joint between the fin and the main body to allow anterior-posterior motion [25]. This unique feature requires a pectoral fin motion such that fin chord at each spanwise cross-section is fairly perpendicular to the rotating motion with little twisting or pitching [25], providing a possible explanation for the high amount of flexibility. Fin deformation is also observed to change with swimming speed [13], but the focus of this section is to study the effect of fin kinematics on the performance at a constant speed.

Although there is considerable amount of observed data for kinematic and performance of ray swimming, little is known about the hydrodynamic principles that give the animal its superior performance. One way to study the hydrodynamics of ray swimming is to isolate the pectoral fin and place it into a water tunnel with constant flow stream to measure the wing performance for various kinematics. The main challenge is to

replicate the exact kinematic motion exhibited by the animal. Specifically, it remains unknown to what extent the animal utilizes its muscles within the pectoral fin to deform its shape (active flexibility) and to what extend the animal leaves the deformation be an outcome of the interaction between the flow and the flexible skin (passive flexibility). Clark and Smits [16] and Dewey et al. [65] performed various experiments to investigate the (wake) conditions for efficient propulsion for an undulating batoid shaped wing.

One way to overcome the difficulty of generating natural fin deformation is to develop a mathematical kinematic model based on the deformation of biological fins and then use the model to study mechanics and hydrodynamics of batoids. The main idea behind this approach comes from the assumption that performance response of two different fins, one biological and one artificial, that undergo the exact same motion is identical without regard to how the motions were generated. Moored [18] developed an analytical three-dimensional model to describe the fin kinematics of Manta ray, where he calculated the fitting parameters by matching the model to the fin kinematics extracted from image processing of biological data. Later on, Russo [75] used the analytical model to study the hydrodynamics of batoid using panel method.

Figure 3.1: Images of (from left to right) manta, eagle and cownose rays, all included in the family Myliobatidae**.**

From computational perspective, two approaches can be undertaken to study the hydrodynamics of flexible batoid shaped fins: (a) Fluid-Structure Interaction (FSI) analysis, and (b) prescribed motion. In the first approach, the deformation of the flexible fin is calculated based on the interaction between the flexible material and the surrounding fluid. This approach is of great use when some part of the fin is actively deformed and it is required to calculate the response of the passively flexible part. In the second approach, it is assumed that the displacement of every point on the fin is known and therefore the fin movement is prescribed. In this approach, the presence of surrounding fluid does not affect the motion of the fin and is driven by it. FSI analyses are computationally much more expensive than the analyses where the motions of the fin is known. Moreover, having an analytical model for the motion of the fin allows the easy integration of the components of motion: for instance, chordwise vs. spanwise flexibility in FSI analyses in which such detailed integrations are harder to perform.

This chapter aims to provide more insight into the effects of kinematics and planform shape on the performance of batoid shaped fins that is often difficult or expensive to pursue otherwise experimentally. First, this chapter presents a computational model for a batoid shaped fin (Myliobatoid family) that is developed to replicate the experimental model built by Moored [18] and validate the computational results. Then, the analytical kinematic model of Moored [18] is used to study the hydrodynamic performance response to different kinematic features of the fin for prescribed motion.

3.1 Fluid-Structure Interaction Approach

Fluid Structure Interaction analysis addresses the set of problems where a fluid domain interacts with a solid domain. Examples include the motion of flexible flapping wings in air or fluid, aircraft wing flutter (aero-elasticity) and deformation of heart valve. FSI analyses are generally divided into two categories in terms of the fluid-solid coupling: (a) unidirectional (one-way) and (b) bidirectional (two-way) coupling. In one-way FSI analysis, the equations for the fluid part are solved without exchanging any information with the equations for the solid part. The motion and deformation of the solid is then solved with the fluid forces as input. In two-way FSI analyses, the information is iteratively transferred between the solid and fluid domain through interface using the kinematic and dynamic boundary conditions. Further information is detailed in chapter 5 regarding the available algorithms and procedures to perform FSI simulations.

The aim of this section is to develop a test case for the validation of the computational results. This validation then provides confidence in the computational method, which is used to further study the hydrodynamics of the rays. A computational batoid shaped fin (Fig. 3.2b) is developed replicating the experimental model built by Moored [18] (Fig. 3.2a). The mechanical prototype was composed of three plates that were hinged at the top and bottom ends with pulleys. The fin motion was generated through pulling opposing cables over each pulley by an actuator. The mechanical setup only allowed motions normal to the surface of plates. The inner structure was embedded inside a flexible skin (made of PVC polymer) to mimic a natural batoid fin. Further details of the mechanical prototype are found in Moored [18].

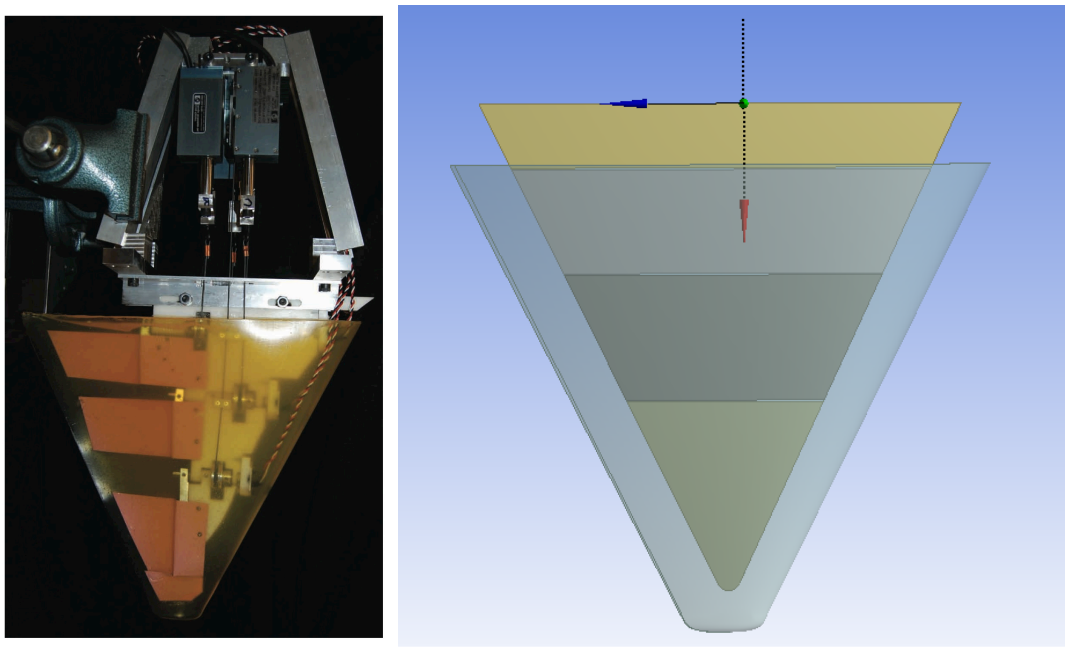

(a) (b)

Figure 3.2: (a) Experimental batoid-shaped fin built by Moored [18], and (b) the computational counterpart.

The experimental inner structure is modeled as three computational rigid plates embedded inside the flexible skin with material properties of PVC polymer, having density $\rho = 1{,}000\, Kg/m^3$, modulus of elasticity $E = 100\, MPa$, and Poisson ratio $\nu = 0.4$. A sinusoidal angular rotation is prescribed at each hinge such that the motion of the computational fin replicated that seen experimentally. Two modes of flapping are considered: (a) flat mode (Fig 3.3b), in which the same sinusoidal function is prescribed for all the hinges, and (b) curved mode (Fig. 3.3a), where maximum angular rotation increases towards the tip to create spanwise curvature. The fin has equilateral triangular planform with a root chord of c = 32 cm and aspect ratio of $AR = 1.47$.

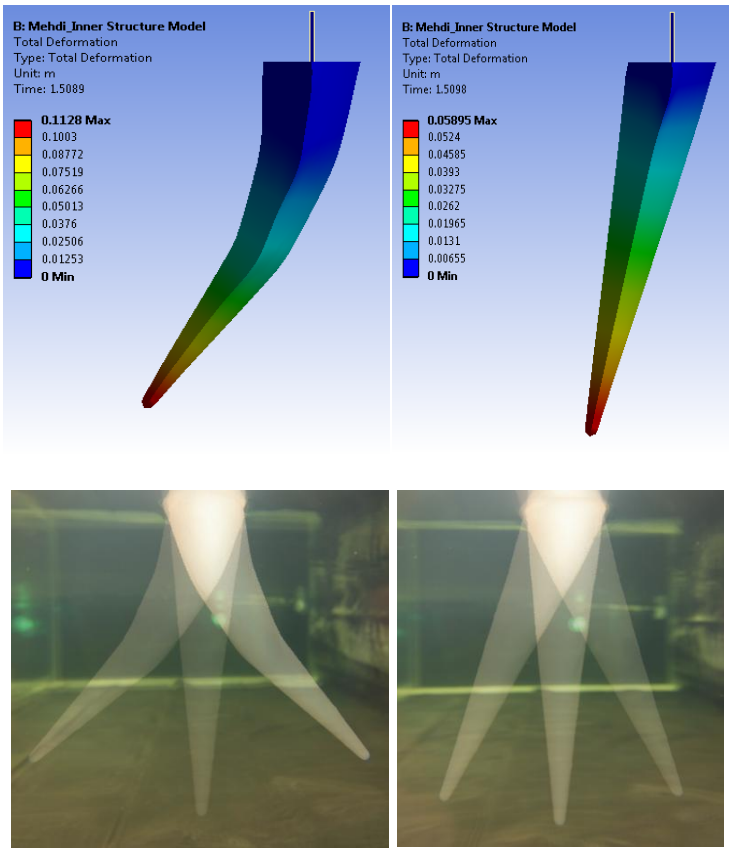

(a) (b)

Figure 3.3: Photos of the (a) curved and (b) flat modes of spanwise flapping for the fin under study. The top photos are computational and the bottom photos are experimental. The flow direction is into the plane of view.

The computational fin model is placed inside a stationary computational domain (a rectangular box) with a fixed incoming flow speed (Fig. 3.4a). The fin root is fixed to the boundary. Swimming (cruise condition) is then simulated by imposing a constant flow speed into the domain. The boundary conditions are defined as follow:

- Inlet: prescribed flow speed
- Outlet: prescribed atmospheric pressure
- Fin-root plane: symmetry
- Side and bottom walls: free slip with zero shear

The dynamic viscosity of the fluid is that of water in 20 degree Celsius, $\mu = 0.0008899\ Kg/m^{-1}s^{-1}$. A typical ray swims at $Re = 10^5$ [25]. However achieving this Reynolds number at laboratory is challenging due to mechanical limitations [18]. Following the experiment, the flow Reynolds number corresponding to the root chord of the fin is set to $Re = 27{,}900$. The Shear Stress Transport (SST) turbulence model [76] is used throughout the study. Details of the numerical procedure are presented in Chapter 5.

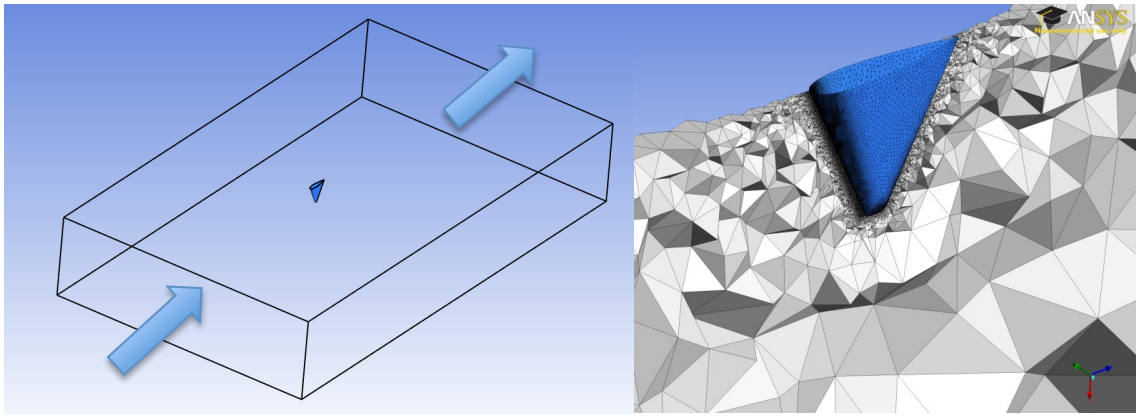

(a) (b)

Figure 3.4: (a) The computational domain under study. The fin root is stationary and fixed to the symmetry plane. (b) Mesh volumes visualized on a plane passing through the mid-plane of the fin.

An unstructured mesh is created around the fin and within the domain. The mesh is refined around the fin and coarsened away from the fin. In particular, the mesh around the leading edge is more refined to capture the dynamic separated flow near the leading edge that is argued to be essential in producing most of the force in flapping propulsion [58]. Due to the excellent match between the computational and experimental results

(Fig. 3.5), no attempt is made to refine the regions that include wake behind the foil. For discussions on the mesh deformation technique, see chapter 5.

The commercial Computational Fluid Dynamics (CFD) package ANSYS® CFX, release 14.0 is used to solve the Navier-Stokes equations for the fluid part on the nodes around the fin and ANSYS® Mechanical is used to solve the continuum equations for the solid part inside the fin (For details regarding the numerical implementations see chapter 5). Both one-way and two-way FSI simulations are performed to investigate the effect of each approach. By matching frequency, Reynolds number and the amplitude (taken as tip-to-tip excursion of the fin) to the experiments, four different St are chosen to perform the simulations. Both flapping modes (flat and curved) are considered. Figure 3.5 compares the cycle-averaged thrust coefficients, $C_T = \bar{T}/\frac{1}{2}\rho U^2 S$ (where S is the planform area), versus Strouhal number for the current computational model against its experimental counterpart. Thrust coefficients were averaged over multiple flapping cycles (at least 6 cycles) to ensure that the transient effects are dissipated.

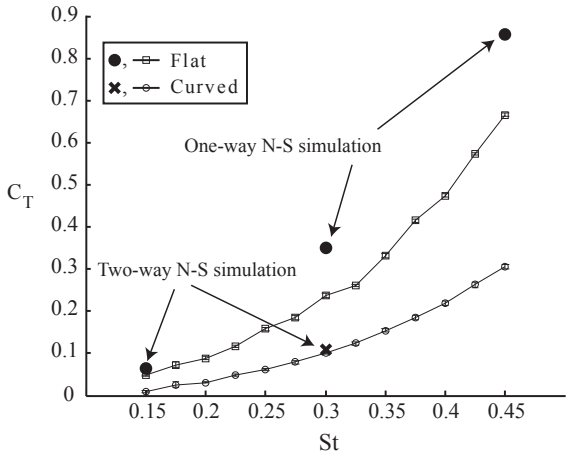

Figure 3.5: Comparison of the computational thrust coefficient as a function of Strouhal number with those obtained experimentally by Moored [18].

As seen in Fig. 3.5, the calculated thrust coefficients are in acceptable agreement with experiment when one-way FSI approach is chosen (less than 35% error) and in excellent agreement when two-way FSI is chosen. Note that the difference between the values for the thrust coefficients calculated by the two approaches magnifies as the fin material becomes more flexible and/or the fin includes more passive flexibility.

3.2 Prescribed Motion Approach

This section presents the results and discussion for the hydrodynamics of the batoid shaped fins when the fin motion is prescribed. The validation of the numerical results against experiment presented in the previous section provides enough confidence in order to use the same mesh and fluid properties to conduct new studies on the fin. Although from computational perspective, two-way FSI analyses are the most accurate

approach to study the fin hydrodynamics, they incur great computational cost and time. As previously discussed, prescribing a known motion on the fin provides more control over the kinematics with less computational cost. The key to minimizing the modeling error is to derive an analytical model that captures the major kinematic features exhibited by batoid shaped pectoral fins through matching the fitting parameters to the biological data.

There is infinite number of analytical forms to describe the deformation of a batoid shaped fin. An example is the model developed by Moored [18] to mimic the deformation of manta ray fins (Fig. 3.6). By mapping the coordinates of the fin at its neutral position to the coordinates of the deformed fin, they derived analytical expressions for the position of each point on the deformed fin as the product of the magnitude of the position vector radiating from the origin and its orientation. Their model captured two major kinematic features: (i) curved spanwise motion, and (ii) chordwise travelling wave. Two constraints were imposed to calculate the parameters: (a) due to the spanwise curl motion of the fin, the magnitude of the position vector, **r**, must be less than or equal to the initial neutral position, x_f, at each time, and (b) the total strain in spanwise direction has to be zero. The final form of the equations derived by Moored [18] is shown in Fig. 3.6c. The fitting parameters (K, m, n, ω) were found by matching the resulting motion against biological data.

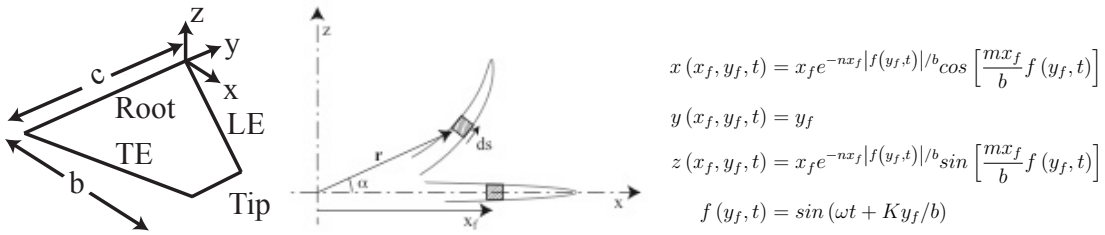

(a) (b) (c)

Figure 3.6: An analytical model was developed by Moored [18] to mimic the Manta ray fin deformation. (a) their fin schematic and dimensions, (b) the differential elements used to derive the equations and (c) the resulting Eulerian coordinates (x, y, z) as a function of the Lagrangian coordinates x_f and y_f.

3.2.1 Planform effect

While the effects of fin geometric taper ratio, TR, defined as the chord length of the tip divided by the chord length of the root (Fig. 3.7), on the aerodynamics of fixed-wing vehicles is well understood, the effects of these geometric features on the hydrodynamics of the flapping wings remain an ongoing research topic. Given the observation that the batoid pectoral fins are highly tapered (with $TR << 1$), it is desired to understand how geometric taper ratio contributes to the swimming agility of the batoid. Here, the model developed by Moored [18] is applied to investigate the effects of planform taper ratio on the performance of a batoid shaped fin that is flapping about its root.

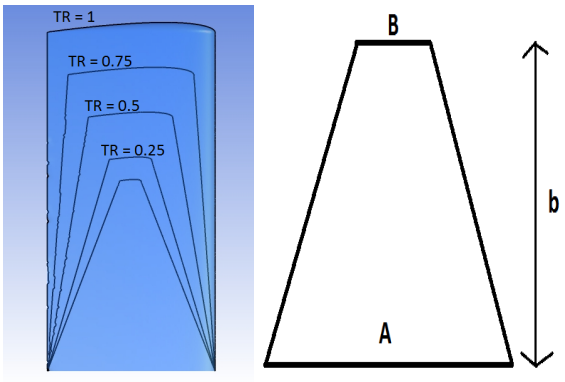

Figure 3.7: Schematic of the fin with different planform taper ratio, $TR = B/A$. Aspect ratio ($AR = b^2/S$) is kept constant during the study.

The fin planform is an equilateral triangle with an aspect ratio (aspect ratio is defined as the square of the wingspan b divided by the area S of the wing) of $AR = 2$. The frequency and tip-to-tip amplitude of flapping are $f = 1$ Hz and $A = 0.8b$ (80 percent of the span, b). The incoming flow Reynolds number based on the mean chord of the fin is $Re = 19{,}000$. The choice of input parameters is based on the swimming kinematics of cownose ray [18]. All the parameters are kept fixed throughout the study but taper ratio remains a variable (Fig. 3.7).

Figure 3.8 plots the cycle-averaged thrust coefficient, C_T, the hydrodynamic power coefficient for power deposited into the fluid, $C_P = \bar{P}/\frac{1}{2}\rho U^3 S$, and the resulting efficiency, $\eta = C_T/C_P$, for the fin under study as a function of the planform taper ratio. The transient hydrodynamic power, P, is calculated as $P = \iint \boldsymbol{F} \cdot \boldsymbol{V}\, dA$ where $\boldsymbol{F}$ and $\boldsymbol{V}$ denote the traction and velocity at each point of the surface of the fin. It is found that both C_T and C_P increase with taper ratio for a given flapping parameters. This increase is mainly attributed to the greater amount of fluid that is being pushed by the fins (normal to the surface) with higher taper ratio (in this case higher taper ratio corresponds to higher

surface area). The increase in thrust with taper ratio comes with the price of consuming more power to flap the fin. The question arises as to whether there is an optimum for the taper ratio at which the resulting thrust is maximized for the given input power, i.e. when the propulsive efficiency is maximized.

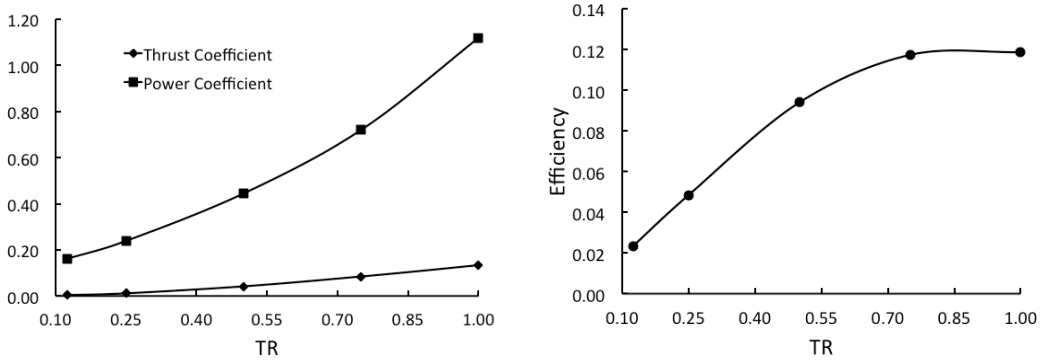

(a) (b)

Figure 3.8: (a) cycle-averaged thrust and power coefficient and (b) propulsive efficiency as a function of taper ratio for the fin under study.

As is shown in Fig, 3.8b, the propulsive efficiency plateaus for fins with high taper ratios. This finding indicates that highly tapered batoid pectoral fins (in nature) are not necessarily adapted for high propulsive efficiency but to minimize the applied toque that is required to flap the fin (hydrodynamic input power). To gain more insight into this finding, transient thrust coefficients are plotted in Fig. 3.9. It is found that during each cycle of the flapping, two peaks of thrust are generated as the fin flaps through the neutral position (when the fin has its maximum flapping speed) and two peaks of drag are observed as the fin comes to rest at the ends of the flapping motion. This expected pattern is similar to that exhibited by a simple 2D heaving or pitching foil. As the taper ratio

increases, the maximum thrust coefficient in each cycle also increases. However, the maximum drag coefficient stays the same without the regard for the value of taper ratio.

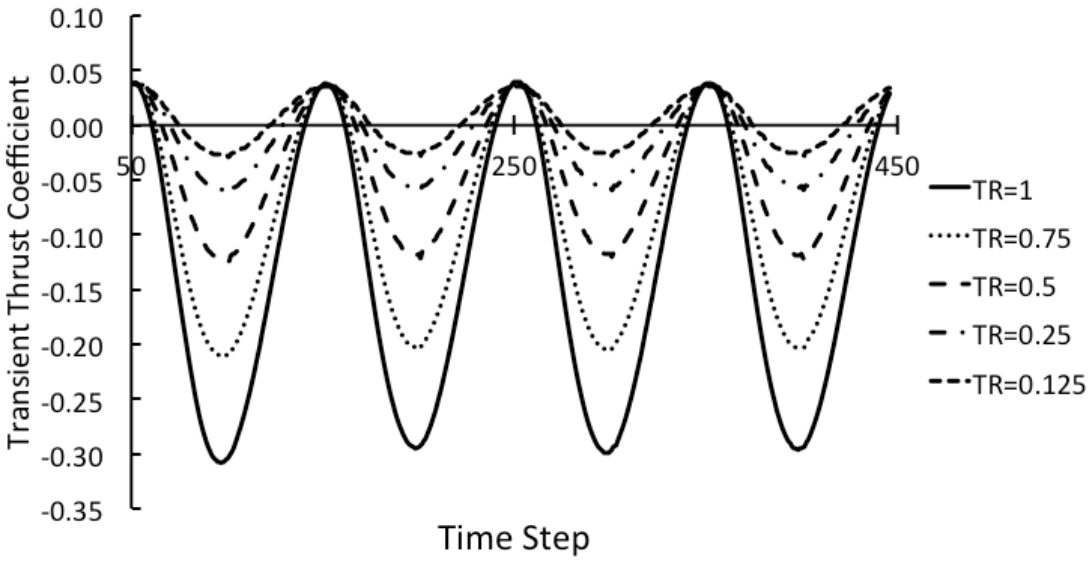

Figure 3.9: Transient thrust coefficient for the last two periods of the run. Note that negative values correspond to force in streamwise direction (thrust) whereas the positive values correspond to force in the opposite direction (drag).

To explain the unintuitive independence of the maximum drag coefficients to the planform taper ratio in each flapping cycle, it is sufficient to think of the flapping fin at the stationary positions as a fixed-wing at which the conventional aerodynamics rules apply (for low flapping frequencies). In the absence of movement and since the fin is composed of spanwise symmetric cross-sections with no chordwise traveling wave, the net generated force on the fin is drag dominated by skin friction. Thus different fins with different taper ratios are considered similar streamlined bodies with different values for drag force (since the surfaces areas are different) however with the same drag coefficient.

3.2.2 The Distribution of Thrust

It is of interest to investigate the distribution of thrust on the surface of the flapping fin. The ultimate thrust distribution affects the structural design of the fin. From experimental point of view, measuring the shear and pressure forces on the surface of a flexible flapping fin is very challenging. Dewey et al. [65] used a control volume momentum integral to estimate the momentum flux just behind the wing in order to find the thrust concentration along the span. They showed that momentum flux is concentrated at a location about 80 percent of the wingspan. Their method however did not account for the pressure change and transverse momentum flux, which are significant in highly three-dimensional flows [52, 16, 77].

Here, the net streamwise force vectors are calculated for the non- and highly tapered fins when the fin has its highest flapping speed (Figs 3.10a and 3.11a). It is found that for both cases, most of the thrust comes from the regions around the fin leading edge towards the tip (as expected also from the quasi-steady theory). However thrust distribution is found to be dependent on the planform taper ratios. For non-tapered fins, thrust vectors are distributed nearly uniformly with two mild spikes, one near the tip and another in about 80 percent of the span (Fig. 3.11a). For the highly tapered fin (Fig. 3.10a), thrust vectors are found to be sharply concentrated near the location at 80 percent of the span. This finding nicely matches with the results presented by Dewey et al. [65], suggesting that ignoring the pressure gradient as well as the spanwise flow terms in estimating the momentum flux behind the fin does not affect the overall qualitative momentum flux distribution.

To take a deeper look into thrust distribution, the surface pressure contours are plotted in Figs. 3.10b and 3.11b for the cases under study. It is clear that thrust vectors are concentrated in the areas with negative gauge pressure (suction). The difference between thrust distributions for non- and highly tapered fins can be explained by considering the effects of tip vortices, which are very strong in the non- tapered fin and weak in the highly tapered fin. Tip vortices create low-pressure regions around the tip of the fin that helps increase the thrust production, however as shown in Fig. 3.8a, come with the price of increasing input hydrodynamic power.

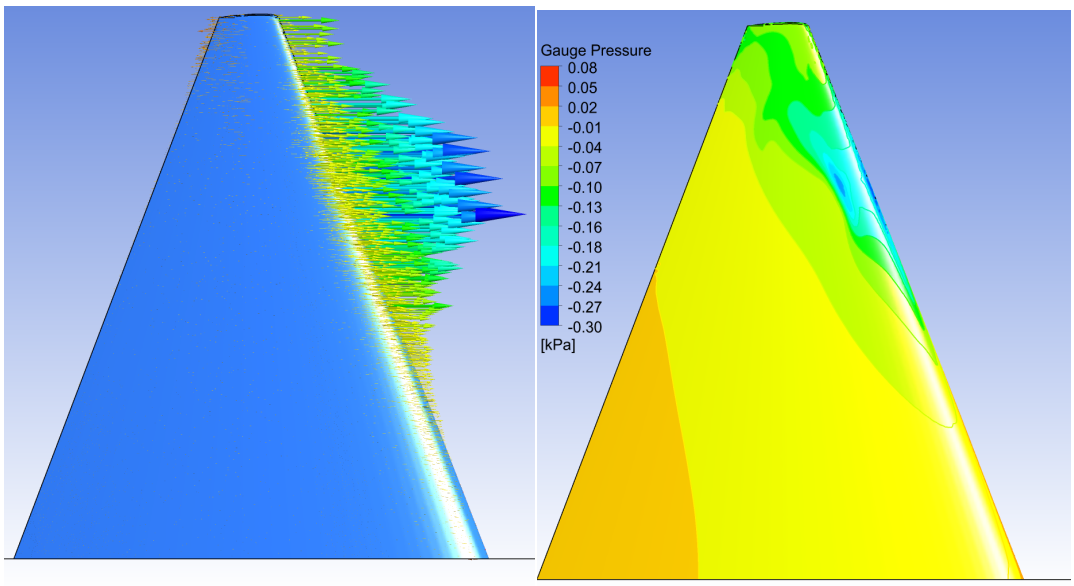

(a) (b)

Figure 3.10: (a) Thrust vetcors, and (b) pressure contours plotted on the surface of the fin with taper ratio of $TR = 0.125$. The fin is at its maximum flapping speed.

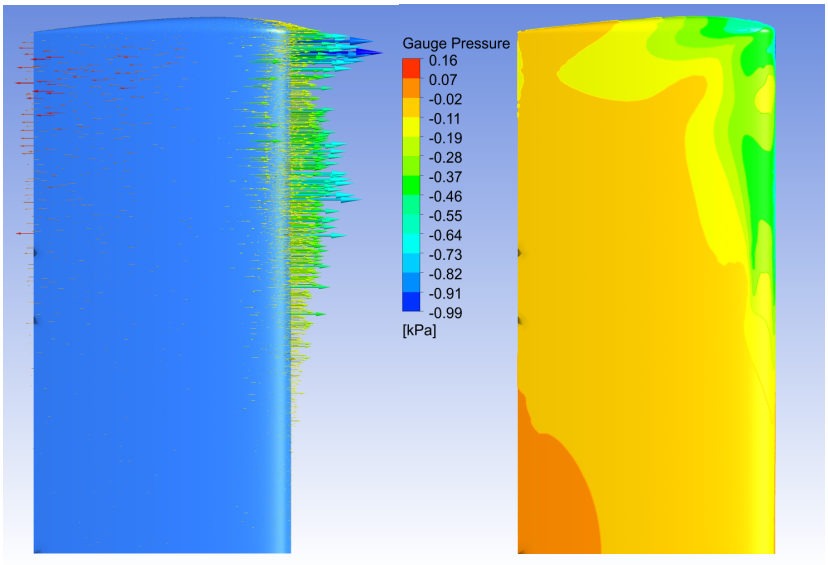

(a) (b)

Figure 3.11: (a) Thrust vetcors, and (b) pressure contours plotted on the surface of the fin with taper ratio of $TR = 1$. The fin is at its maximum flapping speed.

3.3 Wake topology

Computational flow visualization is performed at free-stream Reynolds number of $Re = 10{,}000$ based on the mean chord, frequency of $f = 1.5\,Hz$ and tip-to-tip amplitude of 50 percent of the span. Examining the wake behind the fin suggests a highly three-dimensional flow field. The wake consists of hairpin vortices with alternating signs that originate from the leading and trailing edge of the fin. The structures are similar to that observed by Clark and Smits [16] for an elliptical undulating fin at very low Reynolds number. In this particular case, the direction of the induced velocity arrows suggest that no momentum is being transferred to the fluid, i.e. the thrust produced by the fin is zero. The vortical structures are visualized by plotting the iso-surfaces of Q-

criterion defined as $Q = C_Q(\Omega^2 - K_s^2)$, where C_Q is a constant ($C_Q = 0.25$ in ANSYS CFD-post), Ω is the vorticity magnitude, and K_s is the mean strain rate. The dimension of Q is $1/time^2$.

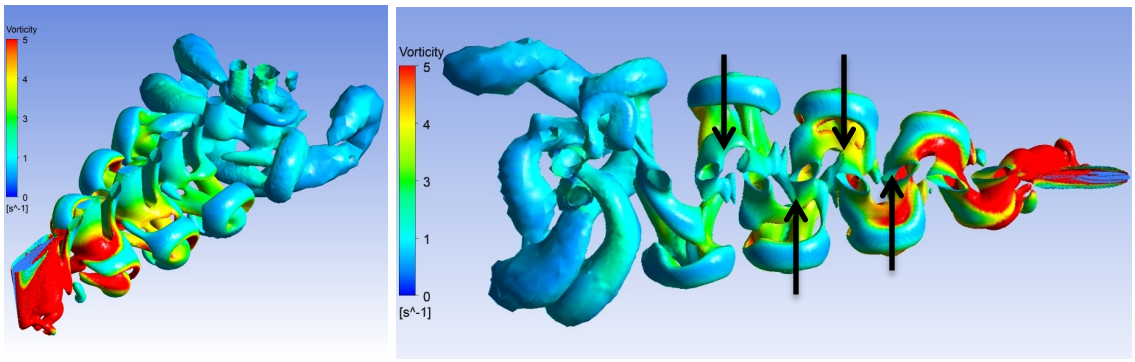

Figure 3.12: Vortical structures behind the computational fin under study. The arrows show the induced velocity direction.

3.4 Parametric Study

To better understand the effects of swimming kinematics on the hydrodynamic performance of batoids, a parametric study is performed to calculate the cycle-averaged thrust coefficient of a batoid shaped fin for a range of flapping frequencies and amplitudes. The planform is chosen such that it mimics the manta ray pectoral fin (Fig. 3.13). The fin root is fixed to the symmetry wall and a fixed-incoming flow speed is imposed on the inlet of the domain (Fig 3.4a). Although manta rays swim with Reynolds numbers close to 10^6 based on the mid-span fin chord [78], the free-stream Reynolds number here is set to $Re = 35{,}000$ considering the numerical accuracy based on the

level of mesh refinement around the foil. Figure 3.13a shows the mesh used for the current parametric study. The analytical model developed by Moored [18] is used to prescribe the fin motion. Large fin deformations were considered to mimic the pectoral fin deformations of manta ray (Fig. 13.14).

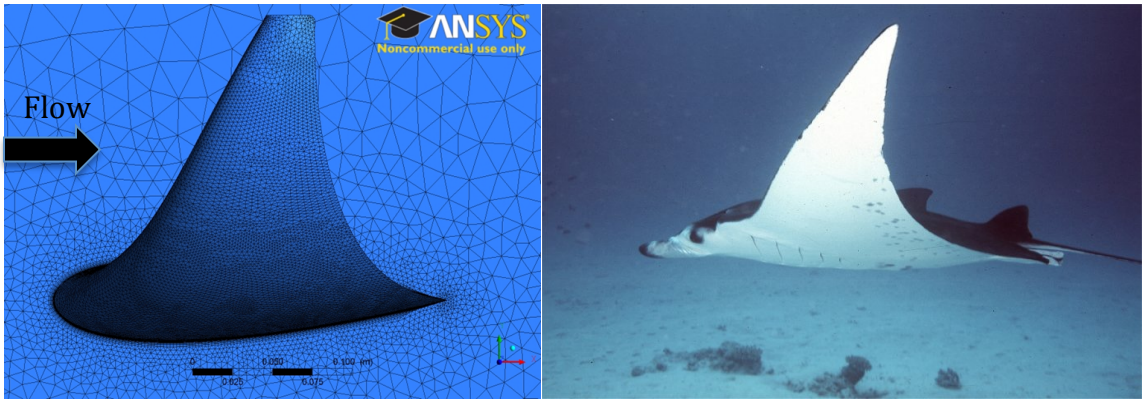

(a) (b)

Figure 3.13: (a) Computational and (b) natural Manta ray pectoral fin.

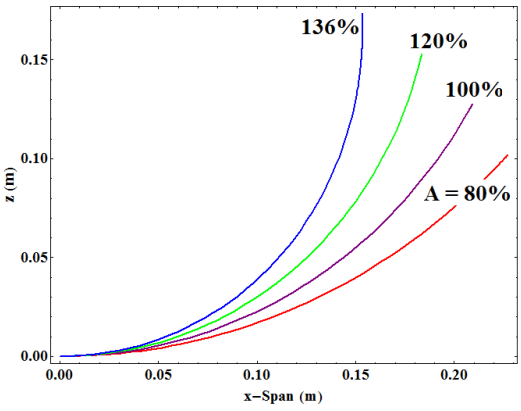

Figure 3.14: Various (front-view) deformation of the fin under parametric study. The amplitude, A, is calculated based on the tip-to-tip excursion.

Figure 3.15a plots the cycle-averaged thrust coefficient as a function of frequency and amplitude (reported as the percentage of the fin span). It is found the thrust coefficient increases with both frequency and amplitude as also found in other three-dimensional [52, 56, 16] and two-dimensional rigid flapping wing analyses [47, 51]. The boundless increase of C_T with f and A without any local optimum is a signature of rigid wing flapping propulsion. Considering that the (curved) motion of the current fin is known, such pattern of thrust coefficient with the kinematics of the fin is expected. For fins that are (passively) flexible, thrust coefficient usually plateaus at some finite frequency and amplitude as shown by Quinn et al. [79].

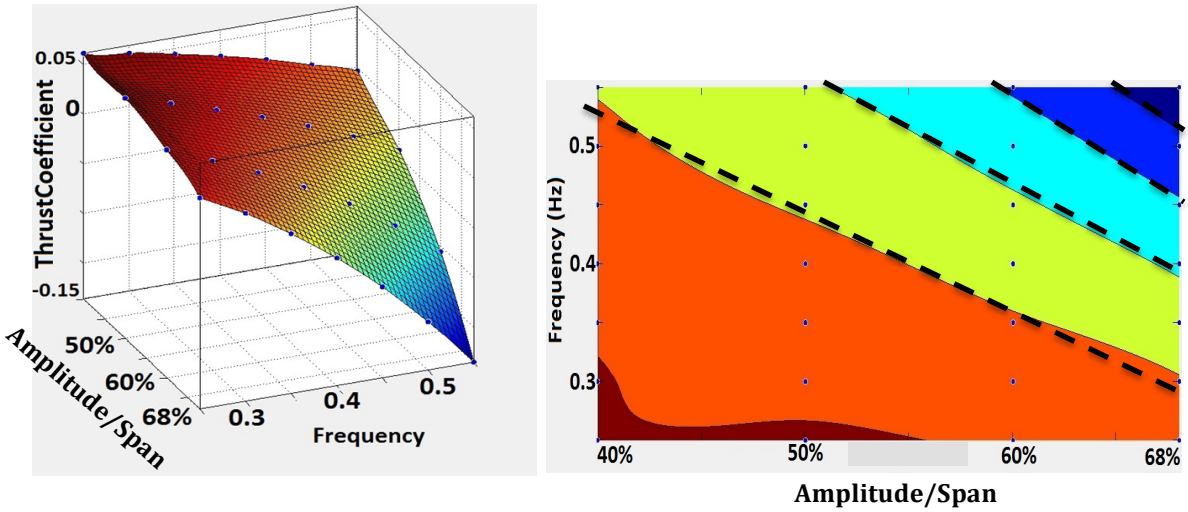

(a) (b)

Figure 3.15: Thrust coefficient (a) surface and (b) contours on frequency versus tip-to-tip amplitude plane. Dashed lines denote constant Strouhal number lines.

Figure 3.15b plots the two-dimensional contours of the thrust coefficient in the frequency versus amplitude plane. Considering the importance of Strouhal number as a non-dimensional kinematic parameter in flapping propulsion, Strouhal number contours

(defined as frequency multiplied the amplitude divided by free-stream flow speed) are also plotted in Fig. 3.15b to see if St helps select an amplitude-frequency optimum for a desired C_T. Interestingly, it is found that the constant thrust coefficient lines (iso-C_T) coincide with constant Strouhal number (iso- St) lines. This coincidence suggests that *thrust coefficient in flapping propulsion can be described solely as a function of Strouhal number. Or, equivalently, for a given* C_T *(and cruise speed) there are infinitely many pairs of amplitude and frequency which results in the same Strouhal number, without regard for energetics of the motion*.

If C_T is indeed solely a function of Strouhal number, then based on the force balance in cruise condition (thrust=drag), it is *implied (hypothesized) that St is solely a function of shape, i.e. drag coefficient and area.* Given the observation that swimming animals cruise with fairly constant Strouhal number for a wide range of speeds [21, 49 and 51], this hypothesis has profound implication on our understanding of the role of Strouhal number in free-swimming. Specifically, there seems to be little relationship between the value of St and the efficiency or economy of the swimmer: St is set by the shape of the freely swimming animal.

Considering the extensive parameter space, high computational cost and the wake complexity of the three-dimensional propulsors, it is decided to investigate this hypothesis and its limits using a simpler propulsion platform. The non-opacity of the model will allow for clearer understanding of the underlying physics. For this matter, a two-dimensional pitching foil is chosen. In the next chapter, a comprehensive computational and theoretical study using the pitching foil is conducted to lay down the

groundwork for providing more physical insight into the meaning of St in free-swimming.

Chapter 4

Two-Dimensional Propulsor

The results of the previous chapter provided clues on how the thrust coefficient of swimming animals is related to their Strouhal number; namely, Strouhal number of a freely swimming animal is apparently independent of its gait. To extend and fully comprehend the implication of this finding on free-swimming, two-dimensional pitching foils are chosen to conduct comprehensive computational and theoretical analyses. First, the relation of St with free-swimming is elucidated. Then, an energy analysis is provided to explain the underlying mechanisms behind the two kinematic commonalities among swimming species, namely the linear relation between tail-beat frequency and speed, as well as constancy of amplitude. Dimensional and scaling analyses are provided to support the computational results.

4.1 A Framework to Study Free-Swimming

Understanding the physical reasons for common kinematic behaviors among swimming fish is of fundamental importance in designing biomimetic swimming robots. One such observed behavior is that animals cruise (and fly) within a tight range of

Strouhal numbers for a wide range of speeds [21, 49 and 51]. Much computational and experimental work has been done to establish the relation between St and the hydrodynamic performance of the flapping fins and foils to explain the possible reasons for this tight range. In such experiments, the foil is typically placed into a water tunnel with a fixed-incoming flow speed and then the thrust and power are measured for different foil kinematics. The measured thrust coefficient usually increases with Strouhal number, but propulsive efficiency peaks for St somewhere between 0.2-0.4 corresponding to the range observed in nature (Fig. 4.1c). Following the experimental results, it has been hypothesized that the maximum propulsive efficiency of flapping motions is the principal mechanism that prompts the swimming animal to *choose* a specific *St* corresponding to the observed narrow range of (0.2-0.4) in nature [(21),(49),(51)]. This tight range has also been attributed to the optimal duration when a leading edge vortex stays attached to produce maximum possible thrust [33].

Although such water-tunnel experiments seem to give clues for how this tight range of St is related to energetics of the swimming, their implication that St is actively tuned by the animal is rather ambiguous. In these experiments, St is considered as an active (input) parameter since the speed is set independently, and is constant. However, in free-swimming of animals, *St* is essentially an outcome (since *U* is a dependent variable). Thus, it remains unclear whether the animal can exercise control over the *St* of the motion to swim efficiently. In particular, the question arises as how to interpret the results of fixed-incoming speed experiments to study free-swimming. There is a final question also that if indeed the animal cannot choose its St, and its St is tuned to the tight range of

optimality, how does this tuning take place, and what aspects of the design of the animal are most responsible for getting this range of the Strouhal number.

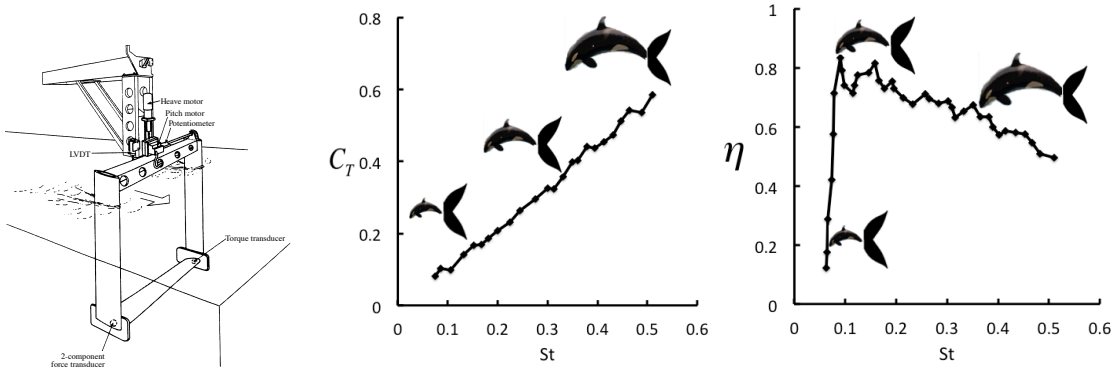

(a) (b) (c)

Figure 4.1 (a) A typical constant-stream approach to studying the hydrodynamics of flapping foils and the measured (b) thrust coefficient and (c) propulsive efficiency as a function of Strouhal number. Different points on the curve correspond to different bodies (source of drag) which are mated with the same propulsor (source of thrust). The curves are adopated from experimental work of Anderson et al. [51].

According to Haj-Hariri [80], there is an inherent inconsistency in constant-stream approach: any measured net thrust other than zero is incompatible with the constant speed assumption. The only proper way to resolve this inconsistency is to assume a finite parasitic drag from a perfectly sized separate body that nulls the measured thrust. Then the system of the propulsor and that body can swim freely at the speed at which the experiment is performed. However, since the speed is constant, different values for thrust correspond to different bodies that are mated to the propulsor under study. This comparison is shown graphically in Fig. 4.1. Thus, the proper way to study free-swimming (for a given swimmer) using water tunnel experiments is to compare motions restricted to specific thrust at a given speed, i.e. look for the best performance of an

actual swimmer whose body and propulsor are already paired, and whose propulsor needs to generate a specific value of thrust (equal to the drag of its body) to maintain cruise at the desired speed.

Assuming that for a given swimmer, source of net thrust and drag can be separated and distinguishable (for instance, in the case of thunniform vertebrates such as cetaceans, tunas and lamnid sharks), a simple model of a fish that consists of a virtual body (as only source of a drag, D) and a propulsor (as the source of cycle-averaged net thrust, $\bar{T}$) is adopted (Fig. 4.2).

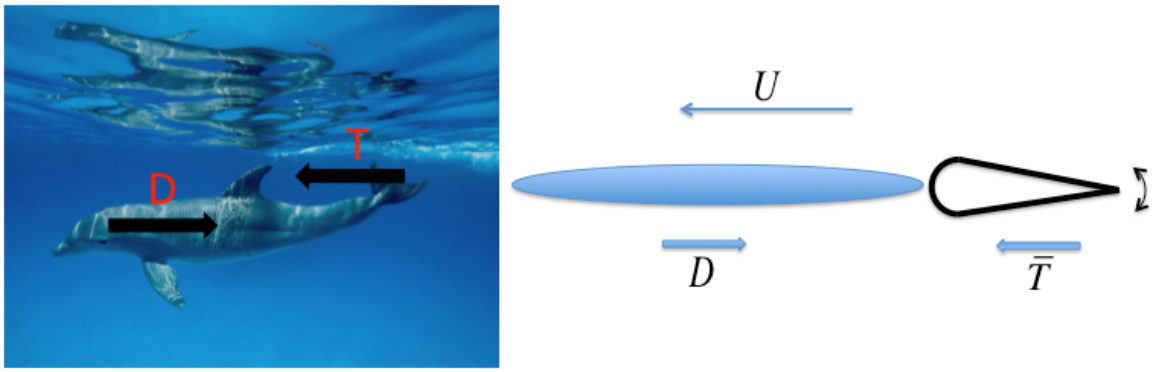

(a) (b)

Figure 4.2: Schematic of a swimmer that consists of a generic body and a rigid pitching foil as the propulsor representing thunniform swimmers. It is assumed that the source of thrust is separate and distinguishable from the source of drag. The flapping motion of the pitching foil is controlled by frequency and amplitude of the oscillation.

This model, although simple, is able to capture the essence of free-swimming. The assumptions leading to the model include:

(a) The proposed model is composed of two-dimensional propulsor and body whereas the flow around a natural swimmer is highly three-dimensional. In three-dimension, area and propulsor planform are

additional major design parameters. Furthermore, three-dimensional propulsors suffer an extra contribution to the net drag (induced drag) due to the presence of wingtip vortices, thus negatively affecting the generated thrust. Induced drag effects are neglected in two-dimensional swimming models. It is expected that the proposed two-dimensional model accurately predicts the fundamentals of free-swimming, i.e. the meaning of Strouhal number, the pattern of which thrust changes with speed, the relation of flapping frequency and speed and the effect of flapping amplitude on the energetics of swimming.

(b) The proposed model utilizes a propulsor with pure pitch motion whereas the caudal fin of a natural swimmer such as dolphin exhibits complex flapping motions (a combination of pitch and heave motions). It is expected that an optimized heave-pitch flapping motion increases the generated thrust for a given input power (higher efficiency) as compared to pure pitch (or heave) motion. However, the fundamentals of free-swimming are expected to remain the same regardless of the type of motion.

(c) The proposed swimming model is based on the cycle-averaged quantities (force and speed) and is constrained to only have longitudinal movement, thus ignores the oscillatory movements (lateral and longitudinal) of a natural swimmer. It is expected that

when such effects are included in the model, higher input power is required to produce the same motion when oscillatory movements were not included.

(d) It is assumed that the body and the propulsor of the proposed swimmer are rigid, i.e. effects of flexibility on the thrust, power and swimming speed are ignored. It is shown that an optimum flexibility increases both generated thrust and propulsive efficiency of flapping foils [79]. It is expected that when such effects are included in the proposed model, more efficient motions can be generated. However the fundamentals of free-swimming are expected to remain the same without the regard for flexibility.

Based on the proposed model, the necessary condition for free-swimming at any cruising speed, U, is stated simply as:

$$\bar{T} = D \tag{4.1}$$

Where $\bar{T}$ is the cycle-averaged net thrust generated by the propulsor and D is the drag force experienced by the body. The non-dimensional form of Eq. 4.1 obtained using the free-stream dynamic pressure is described as:

$$C_T S_T = C_D S_D \tag{4.2}$$

With thrust and drag coefficients defined as:

$$C_T = \frac{\bar{T}}{\frac{1}{2}\rho U^2 S_T}, \quad C_D = \frac{D}{\frac{1}{2}\rho U^2 S_D}, \tag{4.3}$$

where ρ and μ are fluid density and dynamic viscosity, S_T is the planform area of the propulsor (proportional to the propulsor length ℓ_T square) and S_D is the wetted area of the body (proportional to the body length ℓ_D square) with C_D being a function of body configuration and Reynolds number $Re_D = \rho U \ell_D / \mu$. For two-dimensional propulsors and bodies, S_T and S_D are replaced with propulsor chord length, ℓ_T, and body chord length ℓ_D.

In this study a two-dimensional rigid pitching foil with NACA0012 cross section is chosen as the propulsor. A virtual body (a combination of drag coefficient and an area) is considered as a source of drag to nullify the thrust of the foil and allow for cruise at finite thrust coefficients. The foil oscillates sinusoidally about its leading edge. The chord length and the location of the pitching axis are kept fixed throughout the study, making frequency and amplitude of the flapping as well as speed of the incoming flow the only independent parameters. The frequency, amplitude and speed are non-dimensionalized as $f^* = f\ell_T/U$, $A^* = A/\ell_T$ and $Re = \rho U \ell_T / \mu$. Instantaneous power deposited to the flow by the foil is calculated using the method described in Chapter 3. In the particular case of pure pitching motion, transient power can be calculated simply by taking the product of the hydrodynamic moment about the pitching axis and the instantaneous angular velocity. Cycle-averaged quantities are taken over many cycles to ensure that transient effects of starting vortices are suppressed. Each cycle consists of 500

time steps for all the cases. Details of the numerical procedures and validation are presented in Chapter 5.

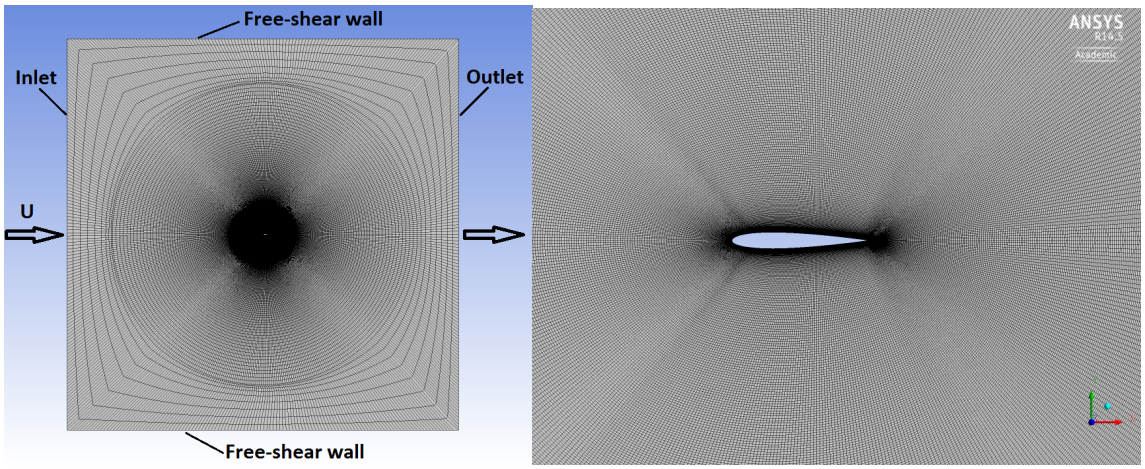

(a) (b)

Figure 4.3: (a) The computational domain with the boundary conditions highlighted and (b) the closed-up view of the mesh around the foil.

The foil was placed inside a rectangular fluid domain (Fig. 4.3a). An O-type structured mesh was created such that it was refined around the foil and coarsened away from the foil (Fig. 4.3b). The physical normal distance of the first mesh node above the surface of the foil was kept fixed for all the cases. The maximum non-dimensional distance corresponding to the first node above the foil surface was $y^+ \approx 2.1$ for the case with the highest Strouhal number, $f^* = 3; A^* = 0.2$, when the foil had its maximum rotational speed. For the mesh study and validation, see Chapter 5.

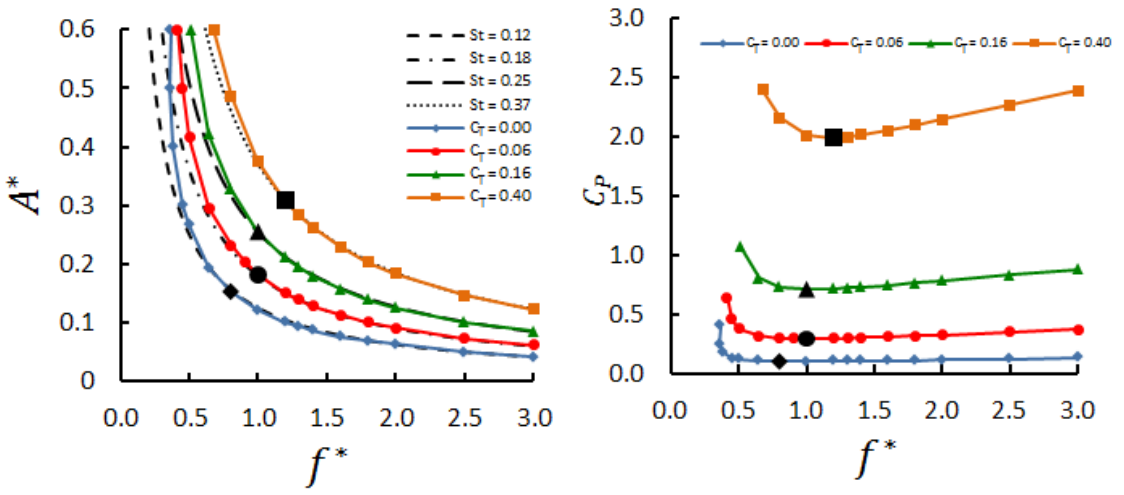

(a) (b)

Figure 4.4: Computed thrust and input power coefficients for the pitching foil under study: (a) C_T contours (solid lines) and the corresponding St contours (dashed lines; $St = f^*A^*$), and (b) power coefficient for each C_T contour as a function of non-dimensional frequency. $A^*_{critical}$ is denoted by bold symbols.

Since the virtual body is identified by an area (a length of the propulsor for 2D cases) and a drag coefficient (i.e. ℓ_D and C_D), then based on Eq. 4.2, each iso-C_T line corresponds to a unique swimmer. In other words, each iso-C_T line relates to the propulsor mated to a specific body. Thus, to properly study free-swimming using the experiments in which the incoming flow speed is fixed, one should compare the motions along individual constant thrust lines. The solid lines in Fig. 4.4a show four contours of C_T $(= 0.0, 0.06, 0.16, 0.40)$ for the pitching foil in the $f^* - A^*$ plane. The Reynolds number for these simulations is set to $Re = 10{,}000$. The dashed lines in Fig. 4.4a show four contours of St $(= f^*A^*)$ $(= 0.12, 0.18, 0.25, 0.37)$, which closely track the C_T contours.

According to Eq. 4.2, each C_T contour in Fig. 4.4a represents a swimmer that consists of a specific virtual body attached to the propulsor under study. Note that

different C_T lines correspond to different bodies attached to the same propulsor such that $C_T \ell_T = C_D \ell_D$, and cruising at the speed at which the numerical experiment is performed. It is interesting to note that C_T and St contours coincide up to some limiting amplitude, $A^*_{critical}$. The amplitude $A^*_{critical}$ is specific to each C_T contour, and is not found to follow any global pattern. Thus for any given swimmer cruising at a constant speed, thrust coefficient depends solely on St of the motion so long as the amplitude is below $A^*_{critical}$. Although initially arrived at for a particular speed U (corresponding to $Re = 10{,}000$), it is found that the phenomenon of coincidence of St and C_T lines in the dimensionless plane of $f^* - A^*$ (Fig. 4.4a) is independent of the cruising speed. This finding is in agreement with the experimental findings of Quinn et al. [79] in which they showed the sole dependence of thrust coefficient of a flexible heaving panel on St over a wide range of conditions. An implication of the sole dependence of C_T on St is that (based on Eq. 4.2) St of the motion for a given cruising swimmer is solely a function of the geometry and drag characteristics of the body so long as $A^* \leq A^*_{critical}$. Kohannim and Iwasaki [81] arrived at the same conclusion without considering the effect of flapping amplitude by solving the kinematic equations for a simple model of carangiform locomotion with three rigid parts and two hinges. For motions with $A^* > A^*_{critical}$, St corresponding to cruise is dependent on amplitude of the motion in addition to the geometry of the swimmer, but our forthcoming studies of the power seem to indicate that this regime is not favored in nature.

The motions along each C_T contour share the same St (for $A^* < A^*_{critical}$), however they vary in terms of power. Figure 4.4b plots the input power for the motions along each of the C_T contours in Fig. 3a. The input power for a C_T contour is found to be

minimum at the point where C_T contour begins to deviate from its corresponding St contour in the $f^* - A^*$ plane, i.e. at $A^* = A^*_{critical}$. These observations are made for a given speed. An important question arises as to how $A^*_{critical}$ (for a given C_T contour) varies with respect to the cruising speed. One way to answer this question is to remain focused on a specific swimmer, i.e. on a specific combination of a virtual body and our propulsor. At each cruise speed, C_T of the propulsor is proportioned to C_D of the body by ℓ_D/ℓ_T. To assess the sensitivity of $A^*_{critical}$ to U, we look at the dependency of body drag coefficient, C_D, on U. This information leads to the dependence of C_T on U, and in turn to the dependence of $A^*_{critical}$ on U. As is shown in Fig 4.7b, drag coefficient of a streamlined body decreases rapidly with flow speed but reaches an asymptotic state at high enough speeds indicating that $A^*_{critical}$ remains insensitive to the cruising speed (for high enough speeds). This finding suggests that the swimmer can minimize its input hydrodynamic power at all speeds by staying at the non-dimensional point corresponding to $A^*_{critical}$ of its St contour. And that this $A_{critical}$ is physically meaningful since it is very insensitive to U. Dimensionally, this means that the swimmer should keep its tail-beat amplitude at a constant level $\ell_T \times A^*_{critical}$ and control its speed by varying the frequency, $f = f^* U/\ell_T$. Our prediction matches the reported behavior for swimming species such as trout, goldfish, shark and dolphin [23 and 24]. For these species the amplitude of the tail beat is constant, and the frequency is proportional to the speed.

4.2 Dimensional Analysis

To generalize the findings of the current study, a dimensional analysis is performed to relate the St of a cruising swimmer to its geometry and kinematics. It is assumed that $S_{D,T} \sim {\ell_{D,T}}^2$. For a cruising swimmer the speed U is an outcome of the motion and is a function of frequency and amplitude of the flapping, as well as geometry and drag characteristics of the swimmer's body:

$$U = \phi(f, A, \ell_T, \ell_D, C_D) \tag{4.4}$$

Nondimensionalizing the above results in:

$$\frac{U}{fA} = St = \phi\left(\frac{\ell_T}{\ell_D}, \frac{A}{\ell_T}, C_D\right) \tag{4.5}$$

Equation 4.5 states that, in general, Strouhal number of a cruising swimmer is a function of shape as well as the amplitude of the flapping. As our power analysis indicates, swimmers should (and do) keep their tail-beat amplitude at a constant level of $A^*_{critical}$ to minimize power consumption at all cruising speeds. Furthermore, this $A^*_{critical}$ is a function of C_T, and in turn, a function of C_D. Thus St of a cruising swimmer, which maintains $A^*_{critical}$, is only a function of shape as described in Eq. 4.6. A somewhat similar dimensional analysis was performed by Wu [82] where he derived the swimming speed of fish as a function of their body length, drag coefficient and metabolic rate.

$$\frac{U}{fA} = St = \phi\left(\frac{\ell_T}{\ell_D}, C_D\right) \quad \text{with } A = \ell_T\, A^*_{critical}(C_D) \tag{4.6}$$

Equation 4.6 highlights the fact that the St at which a swimmer is cruising cannot be chosen by tuning the kinematics of the motion, but is determined once the shape and size of the swimmer are chosen, and the swimmer is set to swim freely.

4.3 Analytical Solution

The dimensional analysis of section 4.2 demonstrates the sole dependence of St on the shape of the cruising swimmer. To motivate how St is related to the drag coefficient and area of the swimmer, Theodorsen's thin airfoil theory is used to derive an analytical solution for the performance of a cruising two-dimensional rigid pitching foil (mated to a generic body) as a function of speed, frequency and amplitude, where the foil is modeled as a flat plate. For a constant incoming flow speed, U, and assuming the flow is always attached on the surface of the foil (i.e. when the amplitude of the motion is small), the total lift exerted on the thin pitching foil when rotating about the leading edge, is composed of circulatory L_1 and non-circulatory L_2 components [45]:

$$L = \pi\rho U\ell_T\, \mathrm{C}(k)\left[U\alpha + \frac{3}{4}\ell_T\dot{\alpha}\right] + \frac{\pi\rho{\ell_T}^2}{4}\left[U\dot{\alpha} + \frac{1}{2}\ell_T\ddot{\alpha}\right] \tag{4.7}$$

$$L = L_1 + L_2 \tag{4.8}$$

In a similar fashion, the instantaneous moment exerted on the pitching axis will be equal to:

$$M_0 = -\frac{\pi\rho{\ell_T}^2}{4}\left\{\frac{3}{4}U\ell_T\dot{\alpha} + \frac{9}{32}{\ell_T}^2\ddot{\alpha} + U\mathrm{C}(k)\left[U\alpha + \frac{3}{4}\ell_T\dot{\alpha}\right]\right\} \tag{4.9}$$

When α is the instantaneous pitch angle and $\mathrm{C}(k)$ is a weak function of reduced frequency known as Theodorsen's function where reduced frequency is defined as $k = 2\pi f\ell_T/U$. The value of $\mathrm{C}(k)$ varies between 0.5 and 1.0, and therefore attenuates the total lift force. The figure 13.19 of Katz and Plotkin [45] plots the exact values of $\mathrm{C}(k)$. The lift components on the foil are shown schematically in Fig. 4.5.

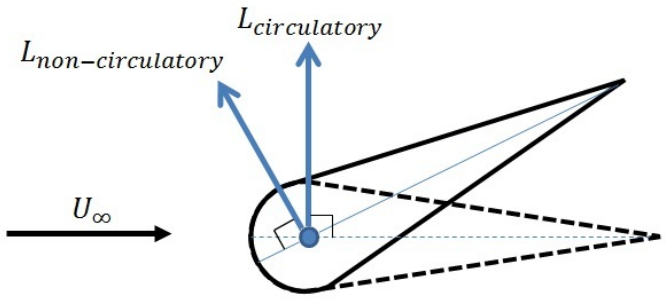

Figure 4.5: The schematic of theoretical circulatory and non-circulatory forces acting on the pitching foil. Circulatory lift is always perpendicular to the free stream velocity as opposed to non-circulatory lift that is perpendicular to the chord of the foil.

*S*ince the circulatory component of the lift is always perpendicular to the free stream direction, L_1 does not have any contribution to thrust production for pitching foils. Instead, non-circulatory effects, i.e. added mass, will contribute to the thrust generated by the foil. As a result, the equation for instantaneous thrust reads as follow:

$$T = L_2\,\alpha = \frac{\pi\rho{\ell_T}^2}{4}\left[U\dot{\alpha}\alpha + \frac{\ell_T}{2}\ddot{\alpha}\alpha\right] \tag{4.10}$$

The instantaneous hydrodynamic power deposited into the flow by an oscillating foil can be described as the surface integral of the inner product of total force and velocity at each point on the surface of the foil. In the case of pure pitching of a rigid foil, the surface integral of the total force times velocity can be simplified to the scalar product of moment about the pitching axis and the angular velocity as shown below:

$$P = M_0\dot{\alpha} = -\frac{\pi\rho{\ell_T}^2}{4}\left\{\frac{3}{4}U\ell_T\dot{\alpha}^2 + \frac{9}{32}{\ell_T}^2\dot{\alpha}\ddot{\alpha} + U\mathrm{C}(k)\left[U\dot{\alpha}\alpha + \frac{3}{4}\ell_T\dot{\alpha}^2\right]\right\} \tag{4.11}$$

Assuming a sinusoidal pitching oscillation, i.e. $\alpha = \alpha_{max}\sin(2\pi f t)$ where $\alpha_{max} = A/2\ell_T$, the mean thrust force and input power over a cycle with the period of $t_P = 1/f$ will be equal to:

$$\bar{T} = \frac{1}{t_P}\int_0^{t_P}\frac{\pi\rho{\ell_T}^2}{4}\left[U\dot{\alpha}\alpha + \frac{\ell_T}{2}\ddot{\alpha}\alpha\right]dt = \frac{\pi^3}{16}\rho\ell_T(fA)^2 \tag{4.12}$$

$$\bar{P} = -\frac{1}{t_P}\int_0^{t_P} M_0 \dot{\alpha}\, dt = \frac{3\pi^3}{32}\rho \ell_T (1 + \mathrm{C}(k))(fA)^2 U \tag{4.13}$$

Therefore, thrust and power coefficients per unit span must read:

$$C_T = \frac{\bar{T}}{\frac{1}{2}\rho U^2 \ell_T} = \frac{\pi^3}{8} St^2, \quad C_P = \frac{\bar{P}}{\frac{1}{2}\rho U^3 \ell_T} = \frac{3\pi^3}{16}(1 + \mathrm{C}(k)) St^2 \tag{4.14}$$

As is suggested by equation 4.14, for pitching foils swimming in an ideal flow at a constant speed with small flapping amplitudes, both thrust and power coefficients can be solely described as a function of Strouhal number. Note that C_P is also slightly dependent on reduced frequency, k, through Theodorsen's function $\mathrm{C}(k)$. This finding highlights the importance of St as a governing parameter in force generation and power consumption of pitching foils. Figure 4.6 compares the computed thrust coefficient as a function of Strouhal number for a pitching foil with NACA0012 cross-section with that obtained using Theodorsen's theory (Eq. 4.14). The Reynolds number and the non-dimensional flapping amplitude are set to $Re = 3{,}000$ and $A/\ell_T = 0.1$. The apparent shift between the two lines in Fig. 4.6 is predominantly due to the absence of viscous drag in the calculations of force and moment in Theodorsen's theory.

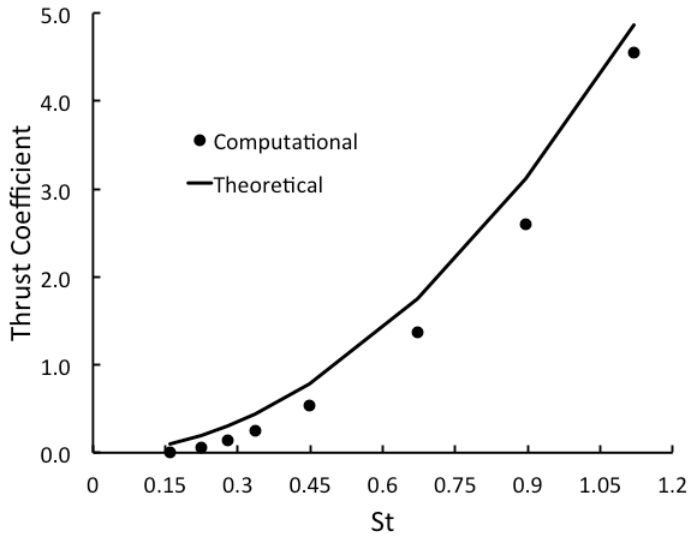

Figure 4.6: Comparison of the computational thrust coefficient as a function of Strouhal number for a pitching foil against the values obtained using Theodorsen's thin airfoil theory (Eq. 4.14).

Consider a two-dimensional virtual body that is attached to the propulsor (with a drag, $D = \frac{1}{2}\rho \ell_D U^2 C_D$) and the system is cruising at some speed U. The value for C_T from equation 4.14 can be substituted into equation 4.2 to satisfy the force balance condition in cruise:

$$\frac{fA}{U} = St = \sqrt{\frac{8}{\pi^3}\frac{\ell_D}{\ell_T}C_D} \tag{4.15}$$

Eq. 4.15 supports the findings that were obtained computationally (Fig. 4.4a) and using dimensional analysis (Eq. 4.6), namely that St is solely a function of C_T of propulsor or C_D of the body. To derive Eq. 4.15, thrust and moment were calculated by integrating the pressure around the thin pitching foil in ideal flow. However, the relation

of St to geometry and drag coefficient of a swimmer can also be obtained using a more general scale analysis. For high flapping frequencies (large f^*) and low flapping amplitudes (small A^*) added mass effects are the dominant contributors for force production. As a result, it makes sense to scale cycle-averaged thrust as $T \sim \rho {\ell_T}^2 (fA)^2$, i.e. base the velocity scale on the normal velocity of the propulsor. A thrust coefficient $\widetilde{C_T}$ corresponding to this scaling is then defined:

$$\bar{T} = \widetilde{C_T}\, \rho {\ell_T}^2 (fA)^2 \tag{4.16}$$

Where it is easy to show that $C_T = St^2 \widetilde{C_T}$. Theory and computations show that $\widetilde{C_T}$ is constant. Based on Theodorsen's theory, for a thin pitching foil in ideal flow, the value for the constant is $\widetilde{C_T} = \pi^3/8$ (Eq. 4.14). For Navier-Stokes solutions, as was shown in Fig. 4.4a, $\widetilde{C_T}$ (and C_T) stays constant for each C_T contour (which is also a *St* contour) so long as $A^* \leq A^*_{crtitical}$; although its value can vary from one contour to another as C_T approaches zero. Substituting the new expression for C_T into Eq. 4.2 results in:

$$St = \frac{\ell_D}{\ell_T}\left(\frac{C_D}{\widetilde{C_T}}\right)^{1/2} \tag{4.17}$$

It has been reported that St for swimming species varies with swimming speed ([3] and [73]). This variation can be explained by noting that based on equation 4.17, St itself is an implicit function of swimming speed through the dependency of drag coefficient of the body, C_D, on the swimming speed (or Reynolds number).

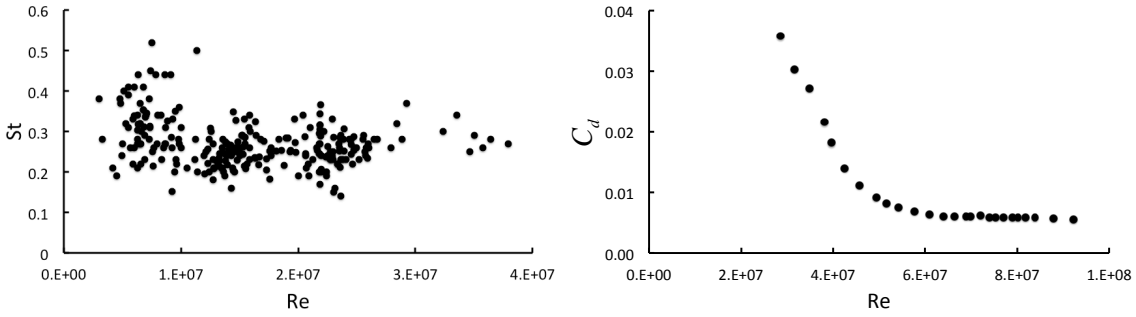

(a) (b)

Figure 4.7. (a) Variation of Strouhal number with body-based Reynolds number for six odontocete cetaceans species observed by Rohr and Fish [24] (private communication) (b) experimental drag coefficient of a streamlined section with 12% thickness ratio as a function of Reynolds number. Adopted from Hoerner [83].

If the values for drag coefficient of two-dimensional streamlined bodies (Fig. 4.7b) are inserted into Eq. 4.17, then St is found to be a decreasing function of swimming speed with a pattern similar to that of drag coefficient (of an streamlined body) with Reynolds number: St drops rapidly with speed at low Re and eventually levels-off (becomes constant) at high enough Re. This trend of St-vs-U predicted by Eq. 4.17 matches closely with that of observed among six captive odontocete cetaceans as reported by Rohr and Fish [24] and shown in Fig. 4.7a.

4.4 Energy Analysis

As was previously discussed, different iso-C_T lines in Fig. 4.4a correspond to different bodies mated to the same propulsor that are cruising at the given speed. Then the question arises as to which of these iso-C_T lines is energetically the most advantageous (in other words, which combination of body-propulsor is energetically the best). As is widely agreed, Froude efficiency, $\eta = C_T/C_P$, is considered as the metric to determine the effectiveness of thrust production with respect to the consumed input power. Thus, the iso-C_T line with the highest overall efficiency is the indicator of a body/propulsor pairing that is capable of swimming most efficiently.

Figure 4.8b plots the efficiency contours for our pitching wing. It is found that there exists one pair of non-dimensional frequency and amplitude ($f^*_{opt} = 1.0; A^*_{opt} = 0.26$) at which the efficiency of the pitching foil attains its global maximum. The existence of this unique point implies that the usual interpretation of Strouhal number ($St = f^*A^*$) as the sufficient indicator of propulsive efficiency [68] is imprecise in a sense that both f^* and A^* are needed to describe efficiency, as also shown by Lewin and Haj-Hariri [47] for rigid heaving foils and later on by Quinn et al. [79] for flexible heaving panels. Nonetheless, the numerical value for the Strouhal number corresponding to the maximum efficiency point is found to be between 0.2-0.4 consistent with what has been observed in nature. We argue that $St \in [0.2 - 0.4]$ is thus not a sufficient condition for optimality (measured by efficiency), but is at best a necessary condition.

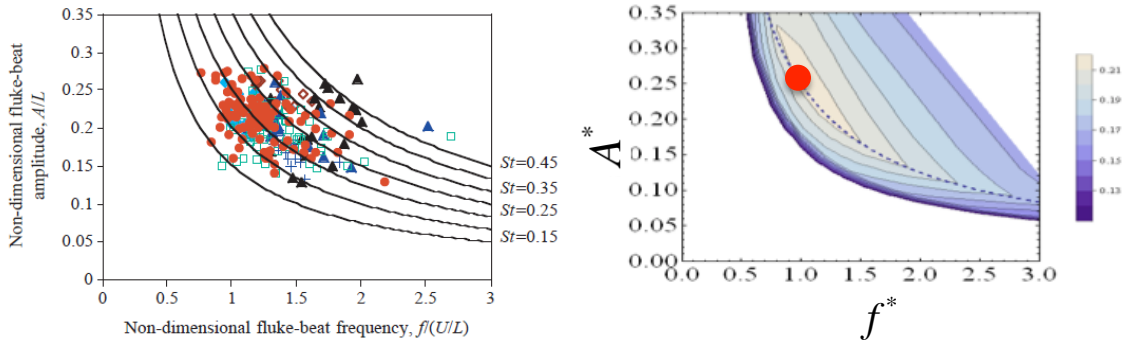

(a) (b)

Figure 4.8: (a) Observed kinematic data points for the captive odontocete dolphins plotted in the non-dimensional amplitude versus frequency plane. Adopted from Rohr and Fish [24]. Note that the body-length is used as length scale. (b) Efficiency contours corresponding to the computations of Fig. 4.4a. The red circle indicates the maximum efficiency point. Note that the propulsor-length is used as length scale.

Our simple model suggests that the swimmer will stay at the maximum efficiency point of its propulsor (at all speeds) when the drag of its body is matched to the thrust of its propulsor at the point of maximum efficiency of the latter. In other words, $A = \ell_T A^*_{opt}$ and $f = f^*_{opt}\, U/\ell_T$. This condition implies that as long as the swimmer controls its speed by maintaining fixed tail-beat amplitude and modulating the frequency, it remains at its optimum design point, and will always swim efficiently. A constant f^* further implies a linear trend between the frequency of the flapping and the swimming speed.

The observations made by Rohr and Fish [24] for odontocete cetaceans, by Bainbridge [23] for few specimens of dace, trout and goldfish, and by Webber et al. [84] for cod (Gadus morhua), confirm the linear trend between the tail-beat frequency of the animals and their swimming speed, as well as the near constancy of flapping amplitude. In particular, the kinematic data points plotted in Fig. 4.8a (Rohr and Fish [24]) clearly shows that the animals are clustered near one point in the non-dimensional frequency

versus amplitude plane, confirming our prediction that both f^* and A^* are bound to a tight range for efficient swimmers.

The iso-C_T lines plotted in Fig. 4.4a (and their corresponding efficiency contours in Fig. 4.8b) are calculated for a specific flow speed. To understand the effect of swimming speed on the maximum efficiency point in Fig. 4.8b, thrust and power coefficients for a set of motions with constant non-dimensional frequency, $f^* = 1.2$, are calculated as a function of Reynolds number (based on the propulsor length) for different non-dimensional amplitudes and plotted in Fig. 4.9. The value of f^* was chosen to be slightly greater than f^*_{opt}. The results are unaffected by the exact value of f^*. The goal of this exercise is to show that the non-dimensional performance parameters are insensitive to the speed. Fig. 4.9 shows that C_T and C_P are effectively constant at high enough speeds (for each amplitude). This verifies that the non-dimensional performance characteristic of pitching foils and their various representations such as the iso-C_T lines or efficiency contours, remain unchanged with respect to swimming speed in the $f^* - A^*$ for high enough Reynolds numbers. Therefore, the optimum-efficiency point $(f^*_{opt}; A^*_{opt})$ is independent of the (high-enough) swimming speed.

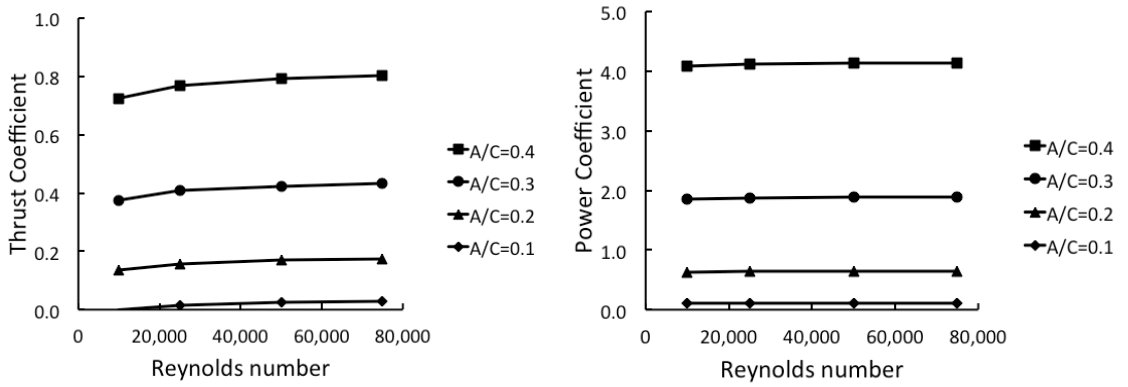

(a) (b)

Figure 4.9: Variation of (a) thrust coefficient and (b) hydrodynamic input power coefficient with Reynolds number for the case with constant non-dimensional frequency of $f^* = 1.2$.

The independence of the optimum design point from the swim speed lends universality to our conclusions: nature is efficient not because the animals are monitoring every detail of their locomotion in real time, but because the design of the animal is such that it cannot be inefficient. Some animals have higher efficiency than others, but each has a body/propulsor pairing, which is optimized for the efficiency of its propulsor. ***And the sophistication of the design alleviates the need for complex control of the motion.***

4.5 Power-Velocity Relation

Power-velocity relation is of great importance in the design and optimization of underwater vehicles as it provides critical information regarding the overall energetics of the vehicles. The goal of this section is to show that the results obtained by fixed-incoming speed experiments are most meaningful when viewed in a more general framework that describes the relationship between the consumed cycle-averaged power inserted to fluid, $\bar{P}$, output power, $\bar{T}U$, and swimming speed, U for a cruising swimmer (a virtual but specific body mated to a pitching foil). The general picture makes applicable to free-swimming the fixed-incoming flow experiments.

Consider a pitching foil (without a body) that is set to swim freely while flapping with a constant amplitude and frequency. The foil is only allowed to move in the streamwise direction. Initially, when the thrust is finite, the foil accelerates from rest. As the foil speeds up it reaches the steady state where thrust is zero (Fig. 4.10). It is of interest to see how the consumed power changes during the acceleration phase. We adopt a quasi-steady view, assuming that the flap period is much shorter than the time scale of variation in the speed. The cycle-averaged input power at each speed, U, is then calculated as if the foil were moving at the constant speed, U. The flapping amplitude is kept fixed at $A/\ell_T = 0.6$ for all the cases reported in this section.

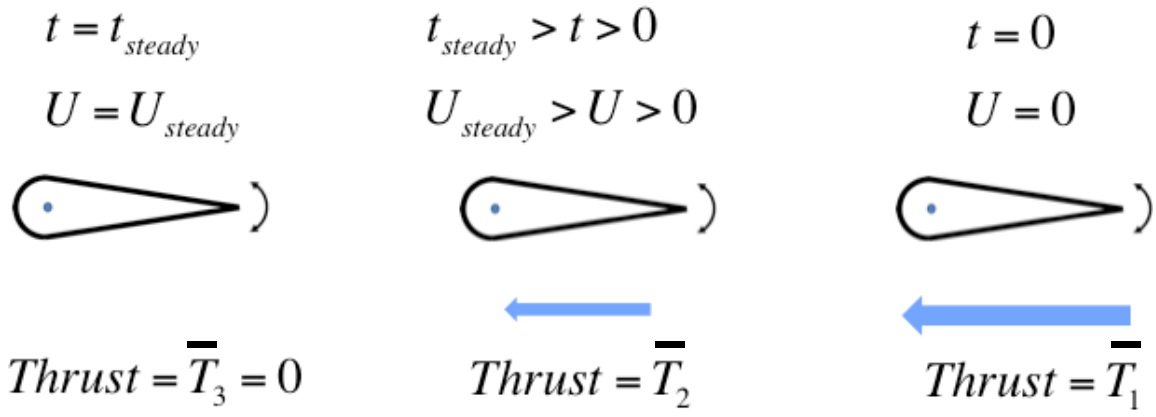

Figure 4.10: The schematic of a pitching foil (constant frequency and amplitude) that accelerates from rest (right) until it reaches the steady state (left).

Figure 4.11a plots the computed cycle-averaged power as a function of Reynolds number (speed) for two different frequencies. For each frequency, the highest Reynolds number corresponds to the speed at which the net thrust is zero (open markers in Fig. 4.11a). It is found that input power remains fairly constant with Reynolds number. Also, as expected, more power is needed for the foil with the higher frequency so that the foil will end up cruising at a higher speed. Note that non-dimensional power, C_P, will behave completely differently than the power itself. Nonetheless, only absolute values for power are of interest in this particular exercise. If the same experiment is performed for many different frequencies, a power-velocity relation can be plotted as shown schematically in Fig. 4.11b. Note that the dashed lines correspond to the (quasi-steady) acceleration phase described in Fig. 4.10. The solid line, which is constructed by connecting the open markers in 4.11a, corresponds to the cruising pitching foil (without a body). Thrust on any point but the solid line is greater than zero.

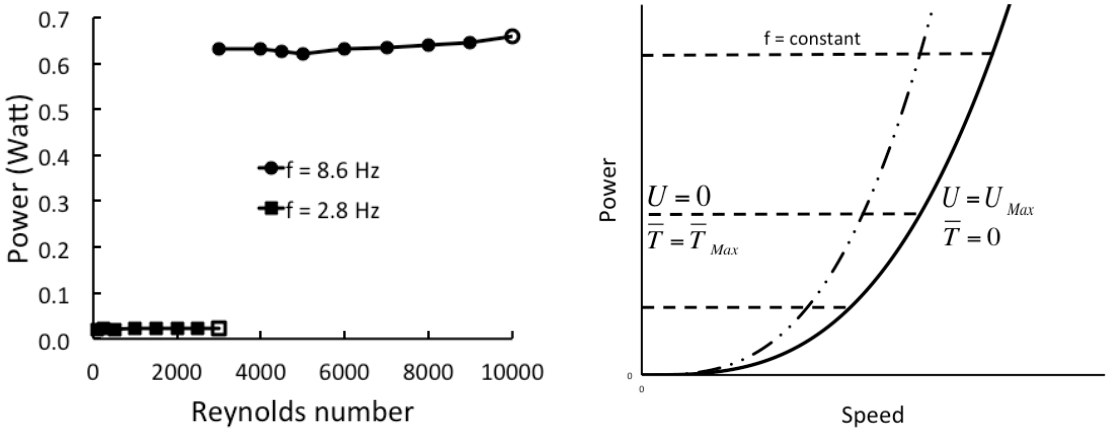

(a) (b)

Figure 4.11: (a) Computed cycle-averaged power as a function of Reynolds number for two given frequencies. Open markers correspond to the speeds where thrust is zero (cruise). (b) the schematic of the final power-velocity relation for a pitching foil if many frequency lines (Fig. 4.11a) are computed. Higher power corresponds to higher frequencies. Solid line corresponds to cruising pitching foil. Long dash dot dot line corresponds to cruising pitching foil attached to a body (drag).

The dependence of the power of a cruising pitching foil on the swimming speed (solid line in Fig. 4.11b) can be obtained simply by stating the input power as follows:

$$\bar{P} = \frac{1}{2}\rho \ell_T C_P U^3 \tag{4.18}$$

As was shown previously, power coefficient, C_P, remains insensitive to the swimming speed at high Reynolds numbers (Fig. 4.9b). Thus, for a cruising pitching foil, the input power increases monotonically as a cubic function of swimming speed.

If a generic body with the drag D ($=\frac{1}{2}\rho \ell_D C_D U^3$) is added to the cruising pitching foil at a given speed U, the pitching foil needs to expend more power (an amount equal to

DU) to swim at the same speed if there were no body attached. The total power for swimmer reads:

$$\bar{P} = \bar{P}_{foil} + \bar{P}_{body} = \frac{1}{2}\rho(\ell_T C_P + \ell_D C_D)U^3 \tag{4.19}$$

It is known that C_D of a streamlined body plateaus to a constant for high enough Reynolds numbers (Fig. 4.7b). Thus, the total power as a function of speed for a swimmer follows the same cubic pattern as that of pitching foil alone (long dash dot dot line in Fig. 4.11b).

Useful power, $\bar{T}U$, is defined as the fraction of the input power that is used to propel forward. For each constant frequency line (horizontal dashed line in Fig. 4.11b), useful power, $\bar{T}U$, produced by the foil is zero at two instants: when the foil begins to swim from rest (since $U = 0$) and when the foil reaches the steady state (where $\bar{T} = 0$). The useful power then must peak at some velocity in between zero and cruise speed. This variation is shown schematically in the three-dimensional plot of Fig. 4.12a. Note that the maximum $\bar{T}U$ approaches zero at the origin. Since the power remains constant along the constant-frequency line, Froude efficiency, $\eta = \bar{T}U/\bar{P}$, follows the same pattern as of $\bar{T}U$ with respect to flow speed. The long dash line in Fig. 4.12a is the locus of maximum efficiency points on power-speed plane.

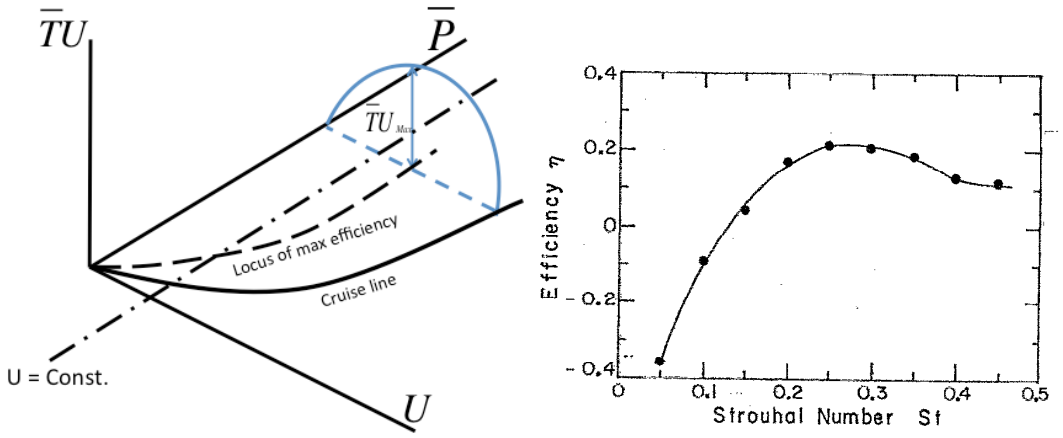

(a) (b)

Figure 4.12: (a) The three-dimensional schematic variation of power input, $\bar{P}$, and useful power, $\bar{T}U$, with swimming speed, U, for a pitching foil. (b) a typical efficiency versus Strouhal number plot obtained from fixed incoming speed experiments. Efficiency plot is adopted from Triantafyllou et al. [49].

The common method of studying the performance of flapping foils is to fix the flow speed (in the water tunnel) and then measure the thrust and power for various frequencies and amplitudes. The constant-speed long dash dot line in the power-speed plane of the Fig. 4.12a embodies the results of such common experiments. Moving along the constant-speed line, thrust and power increase with frequency without bound. Froude efficiency on the other hand peaks at some finite frequency (or St) when the long dash dot line crosses the maximum efficiency line (long dash line on the power-speed plane). This variation of thrust and efficiency with frequency are typical of the performance plots obtained by such experiments (Fig. 4.12b).

The three-dimensional representation of the relationship between power, thrust and speed (Fig. 4.12a) provides useful insight into how the results from fixed-incoming flow experiments should be interpreted for studying free-swimming. To study the free-swimming of the propulsor alone, one should compare the motions along the cruise line

(solid line in Fig. 4.12a). This comparison requires changing the incoming flow speed and then looking for flapping frequencies for which thrust remains zero. In the case of a propulsor that is carrying a body, the motions along the long dash dot dot line should be studied, where the speed for each frequency is such that the resulting thrust of the propulsor balances the drag of the body moving at that speed.

To summarize, Froude efficiency should be used as a design parameter to match a body to the given propulsor. As was shown in Fig 4.8b, for pitching foils, the maximum efficiency occurs at a point in the non-dimensional amplitude versus frequency plane. The correct interpretation of a point in this non-dimensional parameter space is that the swimmer should keep its flapping amplitude at a constant level and change its speed by varying the flapping frequency. This gait then ensures optimal efficiency of the propulsor. For such efficient swimmers, input power increases monotonically as a cubic function of the swimming speed. There does not exist any preferred swimming speed with regard to the input power. In other words, more effort is required for the swimmer to cruise faster. The kinematic data observed among swimming species confirm that the animals do not prefer any swimming speed to another, but rather swim within a wide range of speeds [23, 24 and 84].

4.6 Wake Analysis

The wake properties of two-dimensional heaving and pitching foils have been extensively studied [47, 51 and 53]. However, most of the studies have been usually restricted to low Reynolds number flows ($Re < 1{,}000$). Here, the computational wake

behind the pitching foil is fully analyzed for a wide range of flapping frequencies and amplitudes at high flow Reynolds numbers ($Re = 10{,}000$). The important findings are presented below.

4.6.1 General Properties of the Wake

Figure 4.13 shows a complete set of wakes corresponding to the points (a point is a pair of frequency and amplitude) that constitute the iso-C_T lines shown in Fig. 4.4a. The wake behind the pitching foil is found to consist of simple consecutive array of counter rotating vortices for all amplitudes below the critical amplitude of each iso-C_T line. More complex structures are observed for low flapping frequencies and high amplitudes. In agreement with Godoy-Diana et al. [53], it is found that the transition between von Karman and reverse von Karman wake does not correspond to the onset of thrust generation. In fact the wake transition occurs before the actual drag-thrust transition. Additionally, deflected wake are observed at high Strouhal numbers. The current computational wake patterns are consistent with the experimental observations reported by Godoy-Diana et al. [53] and Schnipper et al. [55].

4.6.2 Wake Pattern at Maximum-Efficiency Point

There have been efforts to determine the wake structures that lead to efficient swimming. In particular, the role of leading edge vortex in attaining high propulsive

efficiencies has been highlighted. For instance, Lewin and Haj-Hariri [47] argued that the maximum efficiency for heaving foils occurred when leading edge vortices coalesced with trailing edge vortices constructively. Similarly, Dewey et al. [65] concluded that high propulsive efficiencies for three-dimensional fins were obtained when the leading vortices merged with the trailing edge vortices over a significant portion of the fin.

In the current study, the leading edge vortex shedding is absent for all the motions of interest owing to the choice of the airfoil (NACA0012) as well as the pitch-only motion. The current computations show that even without the presence of leading edge vortices, there still exists an optimum in the propulsive efficiency of flapping foils with respect to their kinematics (Fig. 4.8b). This raises the possibility that the fundamental mechanism responsible for efficient swimming has its roots in the particular arrangement of the simple counter rotating vortices behind the flapping wing. This remains a topic to be studied in the future work.

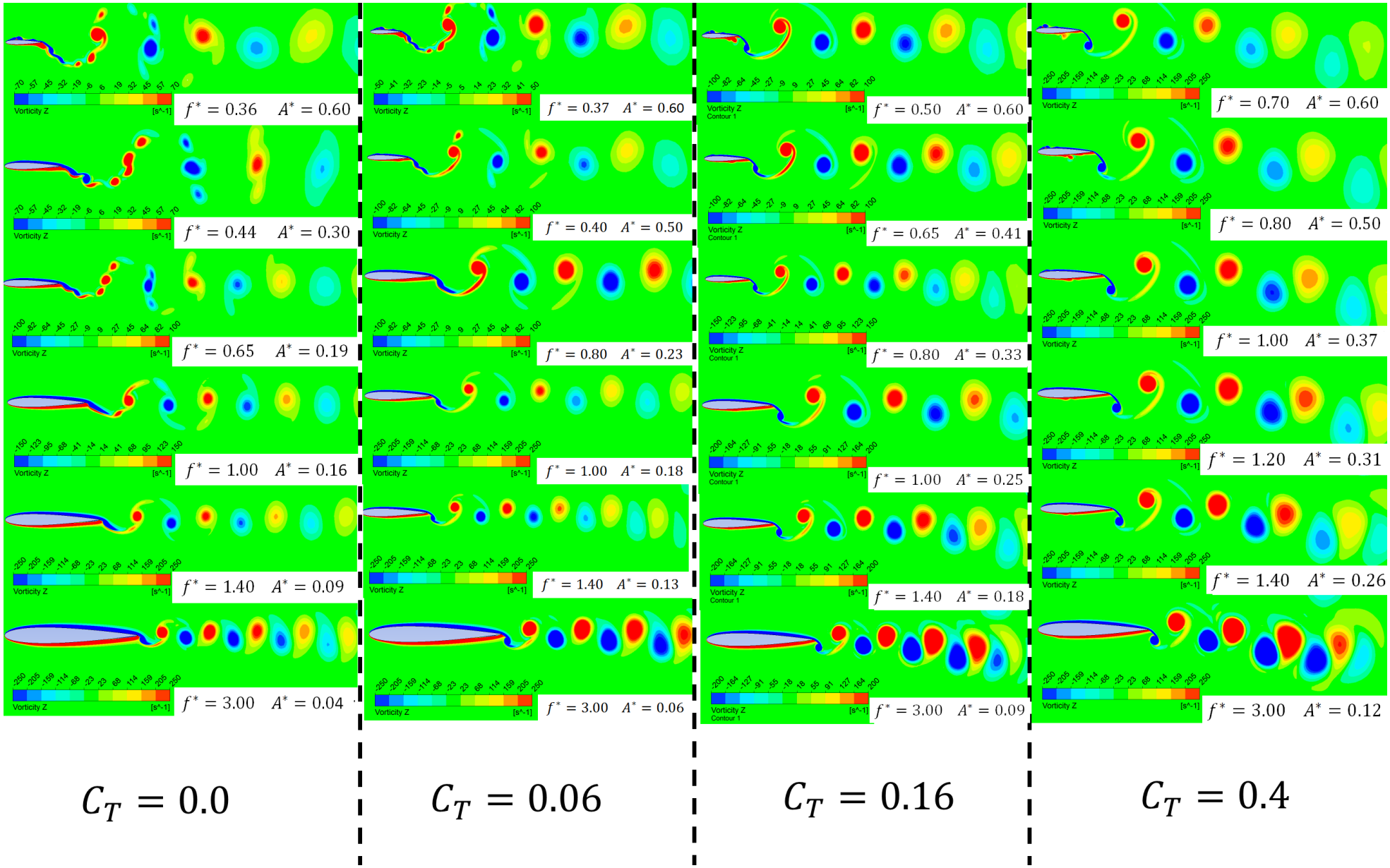

Figure 4.13: Spanwise vorticity snapshots for all the motions along the iso-C_T lines of Fig. 4.4a. Each column corresponds to a specific C_T.

4.6.3 Wake Pattern at Cruise

Of particular interest in studying free-swimming is to analyze the wake evolution behind the swimmer as a function of swimming speed. Fig. 4.14 shows the wake for a self-propelling pitching foil (without body) at different cruising speeds. The flapping amplitude is kept constant at $A/\ell_T = 0.15$ for all the cases (corresponding to the critical amplitude of the iso-C_T line with $C_T = 0$ in Fig. 4.4a). Thus, the foil can be thought as a swimmer that is manipulating the swimming speed by varying the frequency. There are numerous options for determining the physical combination of A, f and U. We proceed by selecting a Reynolds number, and then searching for the flapping frequency that results in zero thrust.

It is found for the first time that the wake structure for self-propelling pitching foils (A=constant) remains fairly unchanged with respect to swimming speed. In particular, the spacing of the vortices remains the same while their strength is modified. One implication of this finding is that the horizontal distance between two consecutive vortices in the wake scales with U/f, which is the non-dimensional frequency, f^*, which remains fairly constant. Although derived for a pitching foil without a body, it is easy to show that the same principle applies to a propulsor that carries a body (drag): once a swimmer is set to swim freely with a constant amplitude, the wake structures remain identical regardless of the cruising speed.

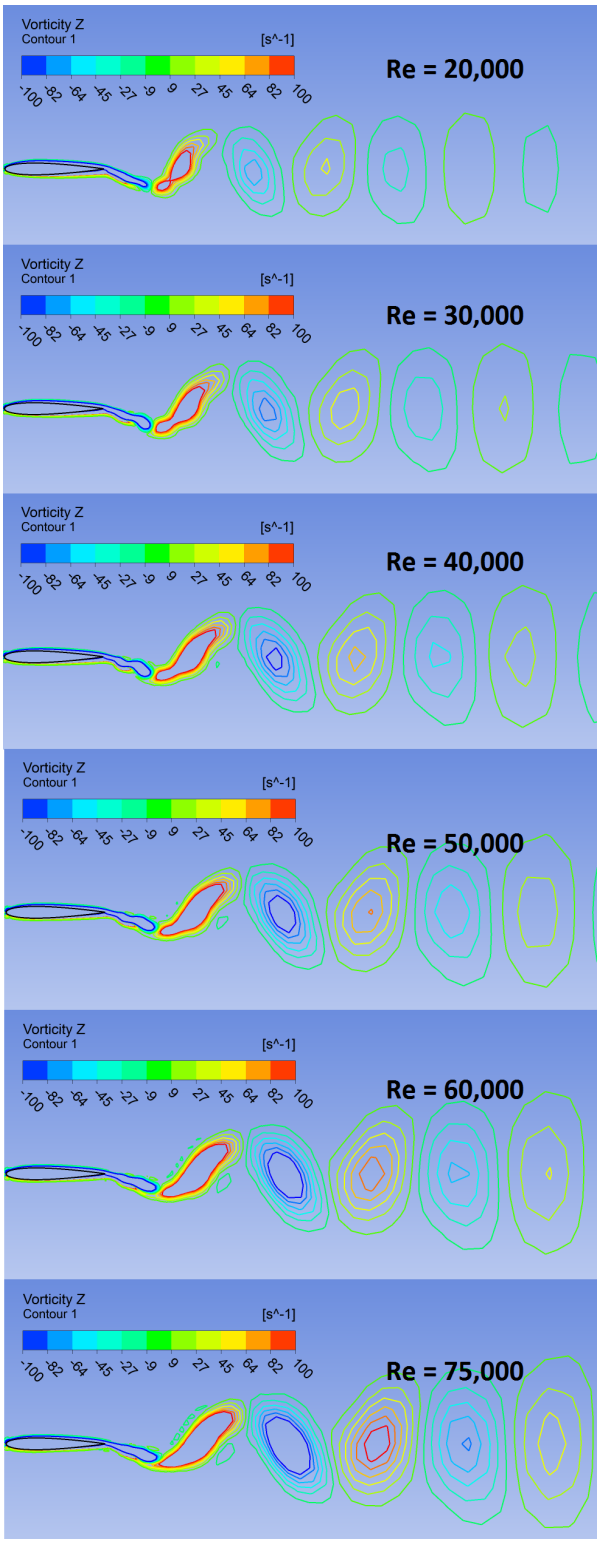

Figure 4.14: Wake pattern behind the pitching foil under study at cruise condition (i.e. when $C_T = 0$) for various Reynolds numbers.

Chapter 5

Numerical Procedures

To address the set of numerical problems discussed in this dissertation, a code is required that is capable of representing complex geometries and performing simulations that include large mesh deformation as well as fluid-structure coupling. For this matter the commercial Computational Fluid Dynamics (CFD) package ANSYS® CFX, release 14.0 was chosen to solve the governing equations for the fluid, while ANSYS® Mechanical was used for the solid part.

The package ANSYS® CFX employs a hybrid finite-volume/finite-element approach to discretizing the Navier-Stokes equations. The Navier-Stokes equations are solved by an unsteady, fully implicit, fully coupled, multigrid solver in the inertial reference frame. ANSYS® Mechanical uses the standard finite element approach to solve for the structure displacement (ANSYS Help system [85]).

5.1 Governing Equations

5.1.1 Flow Equations:

The non-dimensional instantaneous equations of mass and momentum conservation for incompressible Newtonian flows (Navier-Stokes equations) governing all the flows in the current study can be written in the stationary frame as follows:

$$\nabla \cdot \mathbf{u} = 0 \tag{5.1}$$

$$\frac{\partial \mathbf{u}}{\partial t} = -\mathbf{u} \cdot \nabla \mathbf{u} + \frac{1}{Re}\nabla^2 \mathbf{u} - \nabla p + \mathbf{f} \tag{5.2}$$

Where $\mathbf{u}$ and p are the flow velocity and pressure field, Re is the Reynolds number and $\mathbf{f}$ is the external body force acceleration term.

5.1.2 Solid Equations

The structure displacement can be generally described in the Lagrangian form as follows:

$$\frac{\partial^2 (\mathbf{x}-\mathbf{X})}{\partial t^2} = \frac{1}{\rho_s}\nabla \cdot \sigma + \mathbf{b} \tag{5.3}$$

Where **x** and **X** are the current and initial position, ρ_s is the solid density, σ is the Cauchy stress tensor and **b** is the external forcing term.

5.1.3 Solution Strategy

Since there does not exist an analytical solution to the general highly non-linear Navier-Stokes and structural displacement equations, a numerical approach should be undertaken to replace the equations with a set of algebraic equations which can then be solved numerically. To do so, first the conservation equation for mass and momentum must be integrated over each control volume. The volume and surface integrals are then discretized spatially and temporarily within each element. Figure 5.1 shows the schematic of a single two-dimensional element used in ANSYS CFX. The advection schemes can be generalized as:

$$\phi_{\mathrm{ip}} = \phi_{\mathrm{up}} + \beta \nabla\phi \cdot \Delta \boldsymbol{r} \tag{5.4}$$

Where ϕ_{ip} is the solution value at the integration point, ϕ_{up} is the value at the upwind point, $\boldsymbol{r}$ is the vector from the upwind node to the integration point and β and $\nabla\phi$ results in different schemes. In the current study, high-resolution scheme is used for the advection term. In this scheme, the values for β are calculated based on a nonlinear recipe discussed in Barth and Jesperson [89]. Second order backward Euler scheme is used for the transient term. The diffusion and pressure gradient terms are evaluated using

shape functions (a standard approach in finite-element analysis). Fig. 5.2 highlights the general solution strategy taken by ANSYS CFX to solve the Navier-Stokes equations:

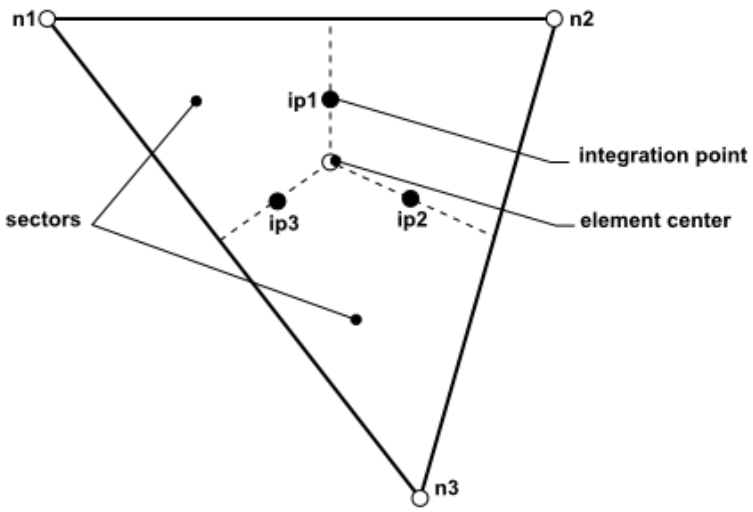

Figure 5.1: Schematic of a two-dimensional mesh element in ANSYS CFX.

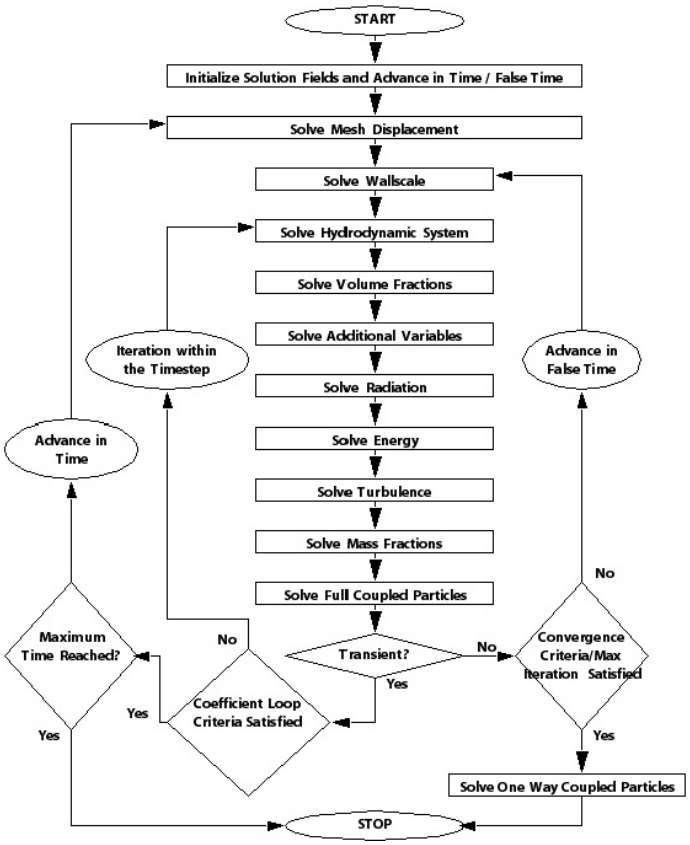

Figure 5.2: The general solution strategy used in ANSYS CFX. Adopted from [85].

5.2 Mesh Deformation

To accurately calculate the normal and shear fluid forces on the surface of the 3D and 2D foils at high Reynolds numbers, body-fitted grids are used throughout this study. When such grids include moving boundaries in the stationary frame, the mesh needs to be constantly adjusted to account for the deformation of the rigid or deformed body. The cases with mesh deformation usually suffer from high mesh skewness issues. A proper way to avoid such problems is to apply the mesh motion gradually where during each

time step the mesh displacement equation is solved iteratively and the results are used to update the new mesh node positions.

ANSYS CFX incorporates displacement diffusion model to tackle mesh deformation. In this model, the position of mesh nodes at the solid surface is known either as prescribed motion or the results of FSI simulation. The mesh motion of all the other mesh points is determined by solving the displacement diffusion equation:

$$\nabla \cdot \left(\Gamma_{\text{disp}} \nabla \delta\right) = 0 \tag{5.5}$$

Where δ is the relative mesh displacement and Γ_{disp} can be thought as the mesh stiffness. Γ_{disp} determines the degree to which the nodes in a specific region move together. Adjusting Γ_{disp} is specifically crucial in avoiding mesh folding near the sharp corners of the geometry such as wing tips. Although a number of models for mesh stiffness are available in ANSYS CFX, the best fit for Γ_{disp} is usually highly problem specific. In the three-dimensional cases studied in Chapter 3 in which the wing underwent high deformations, the mesh stiffness model below was found to minimize the mesh folding:

$$\Gamma_{\text{disp}} = \frac{1}{(d_N + \varepsilon)^5} \tag{5.6}$$

where d_N is the normal distance from the surface of the wing and ε is a constant that is set to 0.001 to avoid singularity of Γ_{disp} at the surface.

For the cases presented in chapter 4, a simplified mesh deformation model was chosen to take advantage of the pure pitch motion of the rigid two-dimensional foil. In

this approach, the domain is divided into three regions as shown in Fig. 5.3: i) The inner circle where a rigid pitch motion is imposed on all the mesh nodes, ii) the annular region where the pitch motion of the nodes linearly drops to zero at the boundary, and iii) the outer region where the mesh is fixed. The radius of the inner circle is large enough to encompass at least 5 consecutive vortices in the wake. This approach eliminates any problem that arises due to mesh folding near the sharp trailing edge of the foil, and leads to higher numerical accuracy (Fig. 5.3b).

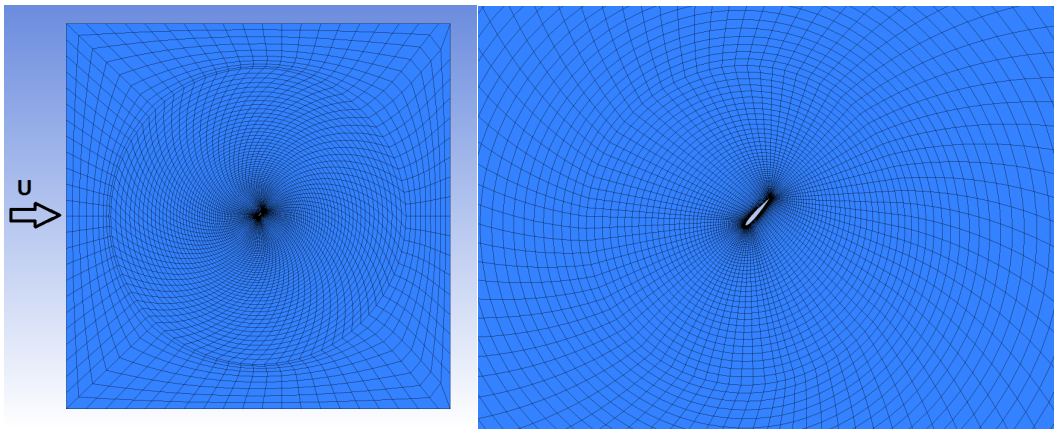

(a) (b)

Figure 5.3: (a) The mesh used for two-dimensional cases is divided into three regions with different mesh motion to avoid mesh folding, (b) the zoomed view of the mesh.

5.3 Fluid Structure Interaction (FSI)

A partitioned approach is undertaken to tackle the two-way fully coupled FSI problems for the cases presented in chapter 3. In this approach, ANSYS CFX flow solver is used to solve the Navier-Stokes equations. The displacement of the solid part is solved using a linear large-deformation transient analysis performed by ANSYS Mechanical

module. The two solvers then transfer the force and displacement data through interpolation at the solid-fluid interface.

The coupling strategy is as follows (Fig. 5.4): for each time step, first the solid solver is run. The calculated loads (pressure and shear forces as well as displacement) are then applied at the interface boundary in the fluid domain before the flow solver starts. These two steps are looped until the final convergence for fluid and solid solver as well as the load transfer is achieved. To ensure a smooth convergence, an under-relaxation factor is used to gradually transfer the loads between the solvers for each time step.

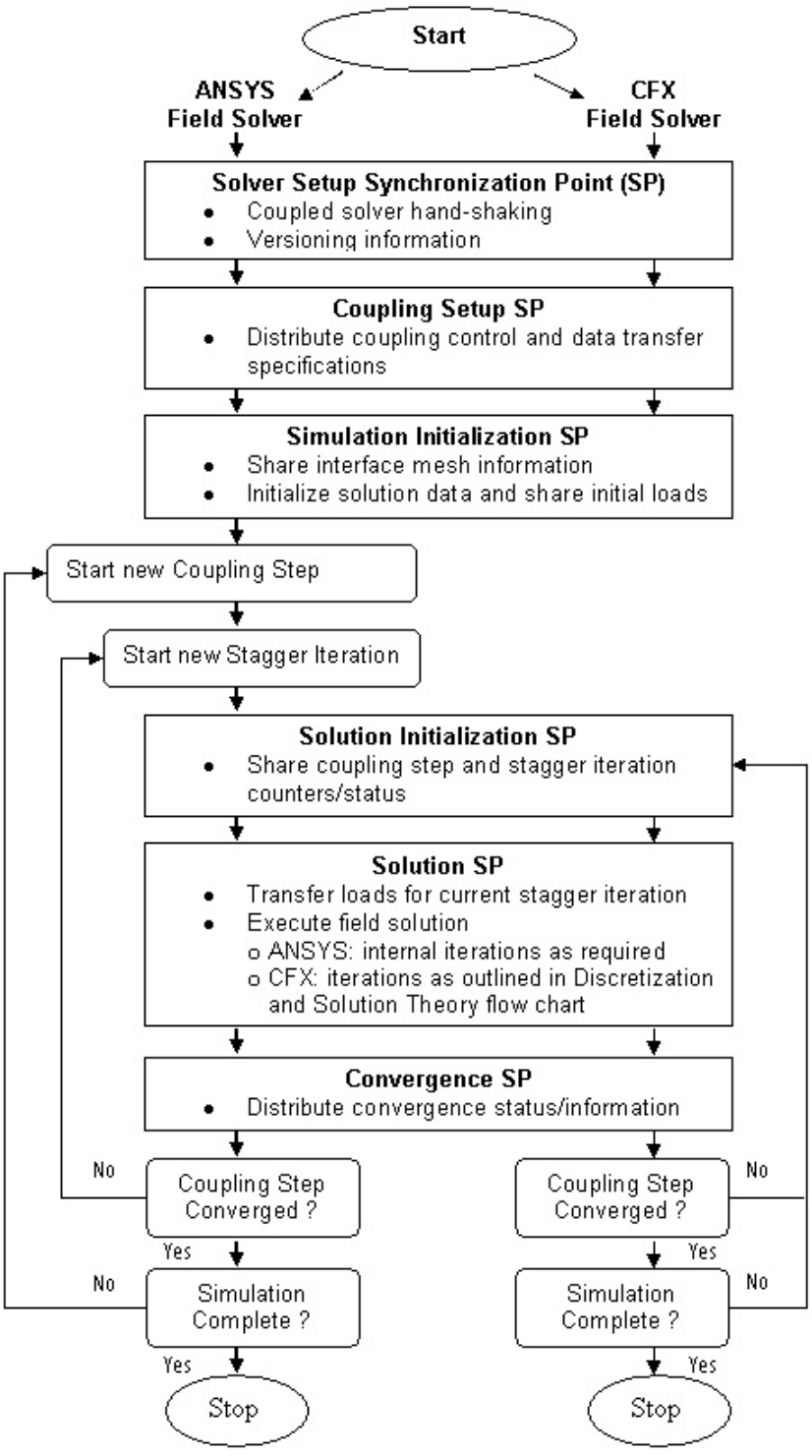

Figure 5.4: The chart that elucidates the steps undertaken to solve a Fluid-Structure Interaction problem. Adopted from ANSYS CFX help System [85].

5.4 Validation of the Flow Solver

The performance and accuracy of the flow solver (ANSYS CFX) is assessed through a series of numerical experiments using steady and flapping airfoils.

5.4.1 Steady Airfoil Section

The flow around two airfoil sections, NACA 0012 and Eppler 387, is simulated for various angles of attack and Reynolds numbers. The Shear Stress Transport (SST) turbulence model [76], which combines the k-ω model near the wall and the k-ε model away from the wall, is used throughout the study. The choice of turbulence model allows for accurate prediction of onset and amount of flow separation under adverse pressure gradient conditions, and provides the ability to handle the laminar-turbulent transition phenomenon. In particular, the SST model allows capturing the laminar-turbulent transition of the separated shear layer over the leading edge of an airfoil. The turbulent shear layer then quickly reattaches to the wall boundary [86]. The reattachment of the shear layer creates a separation bubble along which the pressure is effectively constant. The separation bubble relieves the severe adverse pressure gradient over the airfoil and resists the sudden loss of lift (Fig. 5.5).

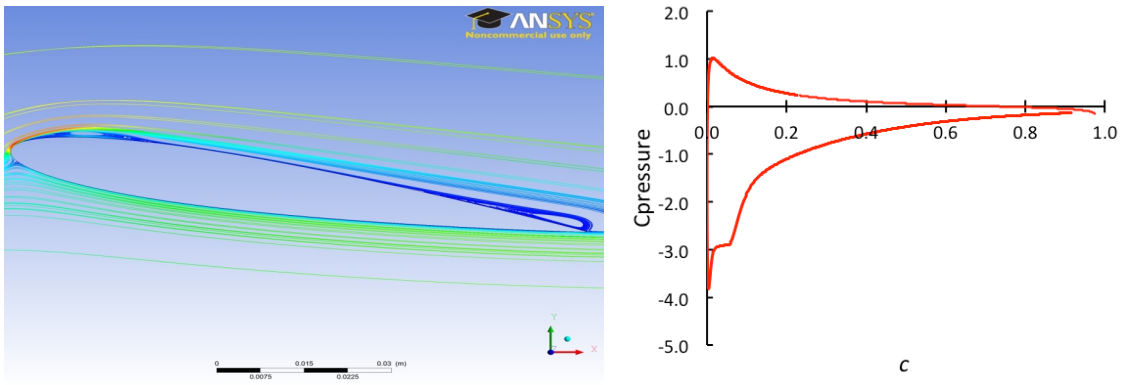

(a) (b)

Figure 5.5: (a) Flow streamlines over a NACA 0012 airfoil section at 10 degrees of angle of attack, and (b) its corresponding chordwise pressure distribution.

The current computational lift and drag coefficients for NACA 0012 airfoil section as a function of angle of attack at $Re = 5 \times 10^5$ are compared against experiment and are plotted in Fig. 5.6. In particular, the stall angle of attack is accurately predicted using the current mesh and numerical setup. Additionally, the computed pressure distribution is validated against experiment for Eppler 387 airfoil section at $Re = 10^5$ and zero angle of attack (Fig. 5.7). Particularly, the pressure along the separation bubble at the aft part of the Eppler 387 airfoil is accurately computed.

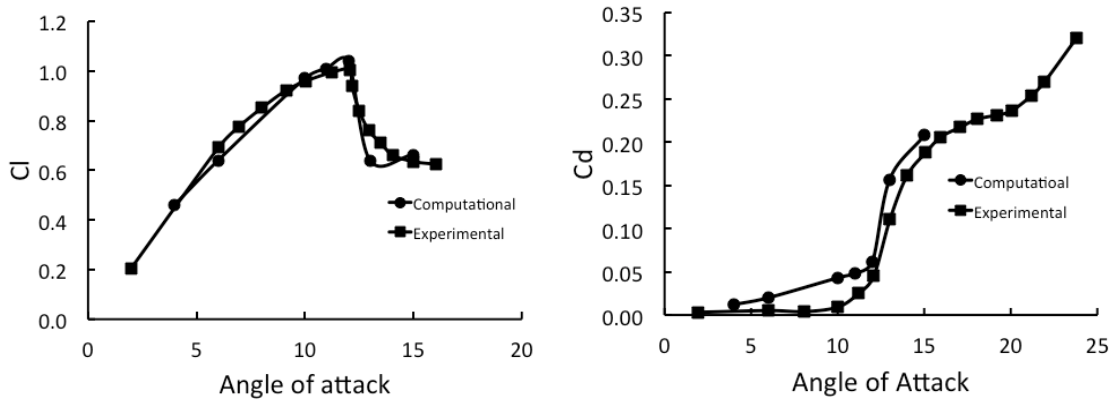

(a) (b)

Figure 5.6: Comparison of the computational section lift and drag coefficients as a function of angle of attack with those obtained experimentally [87] for NACA0012 airfoil.

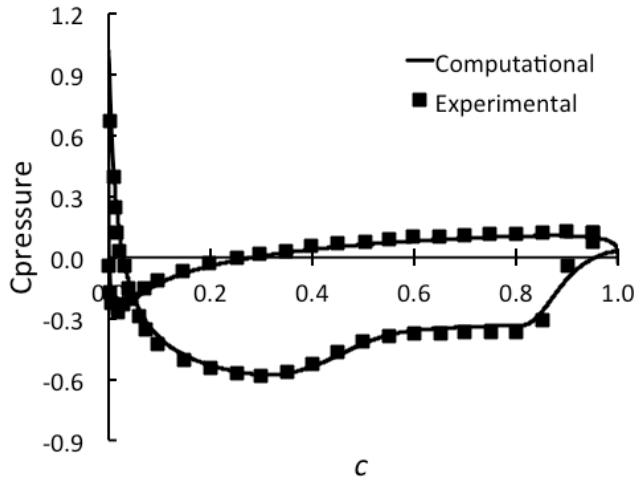

Figure 5.7: Variation of section pressure coefficient over the non-dimensional chord length for Eppler 387 airfoil section at zero angle of attack. The experimental results are adopted form [88].

5.4.2 Pitching Foil

This section presents the numerical details and validation study for the two-dimensional rigid pitching foil discussed in chapter 4. To assess the effects of grid refinement on the solution, three sets of numerical experiments with $(f^*, A^*) = \{(3.0,0.2), (1.2,0.4), (0.8,0.6)\}$ are performed using five levels of mesh refinement: 85×135 (Grid 1 with 85 nodes around the foil and 135 nodes in azimuthal direction), 130×135 (Grid 2), 210×210 (Grid 3), 320×300 (Grid 4) and 480×400 (Grid 5). The Reynolds number is set to $Re = 75{,}000$. Figure 5.8 shows the calculated cycle-averaged thrust and power coefficients for different mesh resolutions. The values for C_T are within 2% of the converged value. The values for power coefficient, C_P, were found to exhibit a similar pattern. The highest grid resolution is chosen to perform the computational experiments reported in the rest of study. To ensure that the computational results presented here are physically valid, the pitching-foil case studied by Godoy-Diana *et al*. [53] is simulated and the computational contour $C_T = 0$ is plotted against the experimental curve in Fig. 5.9. The non-dimensional frequency and amplitude as reported by [53] are converted to match the current scale that uses the chord length as the length scale. The excellent match between our computational results with that of experiment gives confidence in the computational results.

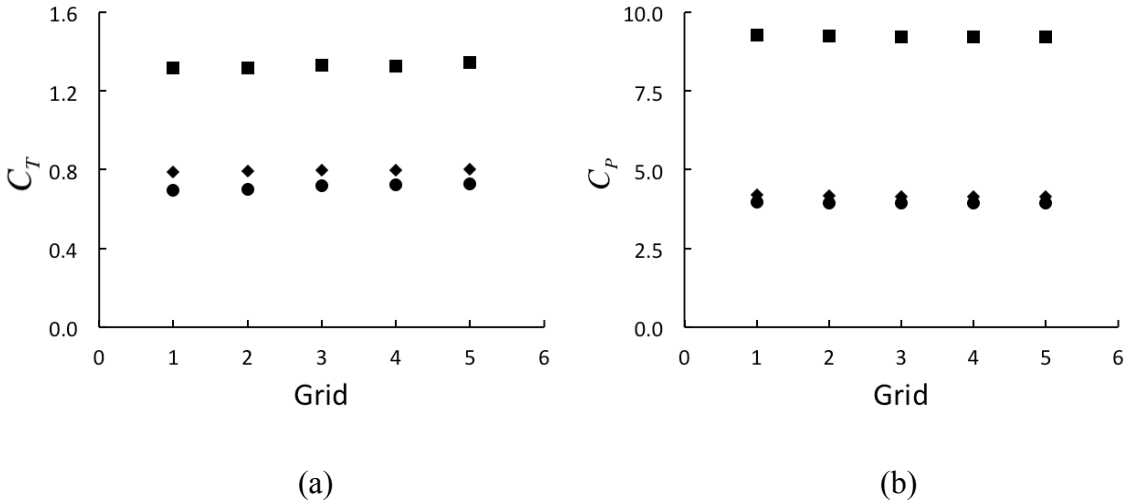

(a) (b)

Figure 5.8. (a) Cycle-averaged thrust and (b) power coefficient for 5 grid resolutions ranging from coarse to fine (refer to the text for the actual resolution) at $Re = 75{,}000$ for (f^*, A^*) values of $(3.0, 0.2)$ ■;(1.2,0.4) ◆; and (0.8,0.6) ●.

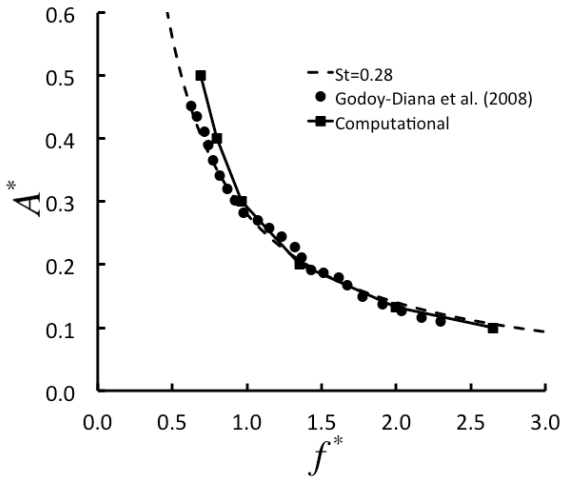

Figure 5.9: Comparison of computational contour $C_T = 0$ with the experimental contour (Godoy-Diana et al. [53]) at $Re = 1{,}173$.

Similar experiment was performed in Gas Dynamics Laboratory at Princeton University in which they measured the performance of rigid and flexible pitching foils with sinusoidal motion in the water tunnel. As an additional step, their case of rigid foil is simulated here. Fig. 5.10 compares the computed thrust and power coefficients against those obtained experimentally. The section of the foil is the same as that of Godoy-Diana et al. [53] with chord length equals to 10 times the leading edge diameter. The flapping amplitude is kept fixed at $A/\ell_T = 10$. The Reynolds number is set to $Re = 4{,}700$. There is excellent match with the experiments, again giving confidence in the computational results underpinning the hypotheses and conclusions in this dissertation.

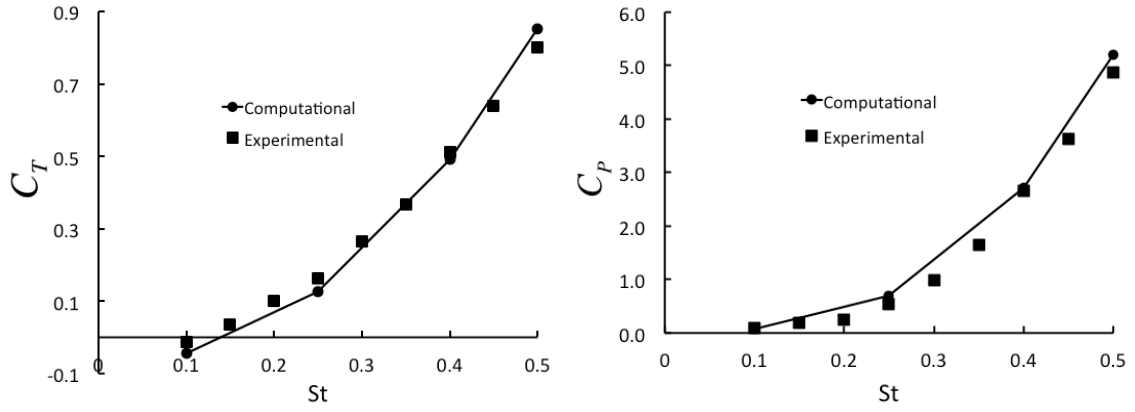

(a) (b)

Figure 5.10: Comparison of the computational thrust and power coefficients with those of obtained experimentally at Gas Dynamics Laboratory at Princeton University. Private communication.

Chapter 6

Concluding Remarks and Suggestions for Future Work

The major goal of this work was to provide new insights into the fundamentals of efficient free swimming. One way to understand animal swimming is to look for the common kinematic patterns among them. Such common behaviors are possible signatures of efficient swimming presumably due to the years of evolution. Two common kinematic behaviors were discussed in this work: (a) the existence of a tight range for Strouhal number among a variety of fish and cetaceans including rays that utilize pectoral-fin-based propulsion and (b) maintenance of a constant tail-beat amplitude by most fish during cruise. They change the swimming speed by varying the frequency such that frequency is linearly correlated with swimming speed. In this research, a computational and theoretical approach was undertaken to study the hydrodynamics of two and three-dimensional flapping propulsors. The prevalent hypothesis to explain (a) was critiqued. Additionally, a physical mechanism responsible for (b) was presented.

First, a three-dimensional model was developed replicating the experimental prototype of Moored [18]. The computational results were validated against experiment to test the accuracy of the mesh and the FSI solver. The effect of planform taper ratio on

hydrodynamic performance was discussed. In particular, the distribution of thrust on the wing planform as well as the wake topology was illustrated. Furthermore, a parametric study was performed to investigate the effects of wing kinematic on the generated thrust. It was found that iso-C_T lines (thrust contour lines) were coincided with iso-St lines (St contour lines) in the plane of (non-dimensional) frequency versus amplitude. This coincidence suggests that thrust coefficient of flapping wings are solely a function of Strouhal number. Since thrust of the propulsor is equal to the drag of the body, this finding implies that Strouhal number of freely swimming animals is predetermined based on the shape of the swimmer, i.e. drag coefficient and area of the body. Considering the large parameter space as well as high computational cost associated with three-dimensional wings, the detailed simulations are focused on a simpler model.

A simple two-dimensional model of a thunniform swimmer was adopted to further investigate the meaning of Strouhal number in free-swimming. The model consisted of a generic body, as the source of drag, and a pitching foil, as the source of thrust. A framework was developed to interpret and adapt the results obtained from today's fixed incoming-flow experiments for studying free-swimming. Within this framework, the performance and energetics of the pitching foil were computed and discussed. An analytical solution was also derived for the performance of pitching foil using thin airfoil theory. Dimensional and scaling analyses were performed to generalize the findings. Wake evolution behind the pitching foil was fully discussed. The two-dimensional results were validated against experiments performed at Gas Dynamics Laboratory at the Princeton University. Lastly, the numerical procedures employed to

compute the performance of two and three-dimensional flapping foils were presented. The important findings of this research are summarized as follows:

(a) The interpretation of *St* as a sufficient measure of efficiency is too broad. This finding is in contrast to the previous hypothesis that suggests the tight range of St dictates the efficiency of the motion ([21] and [49]). Underpinning this assertion is the observation (presented in this dissertation) that in free swimming the Strouhal number of the motion for a given swimmer is effectively fixed for all gaits, including those that may be inefficient. In fact, it was shown here for the first time that St is only a function of shape, i.e. drag coefficient and area of the body. The constancy of *St* in free swimming follows simply from the observation that in free-swimming the speed (and thus *St* indirectly) is a dependent variable.

(b) For a given swimmer, St is a decreasing function of swimming speed with a pattern similar to that of variation of drag coefficient with Reynolds number for streamlined bodies: they both decrease rapidly with speed and level off for high enough swimming speeds. The trend closely matches that exhibited by 248 captive odontocete cetaceans reported by Rohr and Fish [24].

(c) For a pitching foil oscillating with sinusoidal motion, there exists a unique optimum point in the dimensionless frequency ($f^* \equiv f\ell_T/U$) vs. amplitude ($A^* \equiv A/\ell_T$) plane, where Froude efficiency is maximized. It is found that this point is insensitive to swimming speed for high enough Reynolds numbers. In

free-swimming, the maximum efficiency point represents a swimmer with a generic body whose drag is perfectly matched with thrust of the pitching tail under study so as to place the swimmer at the optimum point of the performance of its thruster. So long as the swimmer controls its speed by maintaining fixed flap amplitude and modulating the frequency, it remains at its optimum design point, and will swim efficiently. This finding gives physical explanation for the observed kinematic behavior among seven different cetacean species reported by Rohr and Fish [24] and for few different fish species reported by Bainbridge [23]: Swimming animals such as trout, dace, goldfish, cod and dolphins cruise by oscillating their tails with fixed amplitude while controlling swimming speed by modulation of their tail-beat frequency such that speed is linearly correlated with frequency.

a. In free-swimming, the location of maximum efficiency point in $f^* - A^*$ plane changes with swimming speed for low Reynolds numbers (due to the dependence of body drag coefficient on Reynolds numbers). Thus cruising animals should (and do) change their flapping amplitude at low swimming speeds to stay at the maximum efficiency point. This finding gives an explanation for the question posed by Webb [74] as to why the swimming animals do not maintain their tail-beat amplitude at a constant level when swimming at low speeds.

(d) For swimmers that are designed based on the maximum propulsive efficiency point in $f^* - A^*$ plane (i.e. their body is perfectly matched with their propulsor), the power inserted to the flow by the propulsor increases monotonically with respect to the swimming speed. In other words, for a swimmer that is cruising with some constant amplitude, there does not exist an optimum swimming speed based on the power, and simply more effort is required for the swimmer to cruise faster. Evidence supporting this finding is found from the swimming kinematic data provided by Rohr and Fish [24] for dolphins and Bainbridge [23] for a number of fish species where it is observed that fish swim within a wide range of speeds without preferring one to another.

(e) It is shown (for the first time) that the wake structure for a cruising swimmer that keeps the tail-beat flapping amplitude constant while changing the speed by manipulating frequency remains unchanged with respect to cruising speed. This observation implies that there may exist a specific arrangement of vortices in the wake that is energetically superior over the others. This could be related to the wake stability studies by Lewin and Haj-Hariri [47], Moored et al. [67] for rigid foils and Moored et al. [91] for flexible foils.

Future work

The findings of the current work were derived using a simple two-dimensional body-pitching foil fish model that allowed us to learn the fundamentals of efficient

swimming. Within the current framework, it is of interest to study free-swimming using more complex models. The future steps that can be undertaken to expand our knowledge of efficient swimming are summarized as follows:

(a) *Complex flapping motion*. The heave motion can be added to the current pitch motion to make up a more complex flapping motion. Pitch-heave motions can acquire high propulsive efficiency compared to heave or pitch-only motions (Anderson et al. [51]). The parameter space corresponding to such motions is large and is composed of frequency, pitch and heave amplitude, speed and phase angle between heave and pitch. The pitch-heave motion also generates more complex wakes that do not necessarily follows a particular pattern (specially due to leading edge shedding).

(b) *Three-dimensional model*. In 3D swimming models, area and planform shape of the propulsor are additional major parameters. An objective will be to find the best wing platform that produces more thrust with less/equal input power among others. Nonetheless, it is expected that in 3D, the swimming fundamentals that were discussed in this research remain unchanged.

(c) *Swimming with no constraints*. In this research, fish swimming is simulated by fixing the model and imposing a constant flow stream into the domain. However in reality, a fish that is swimming freely along a straight line, exhibits oscillatory movements in streamwise and vertical directions due to the oscillatory nature of

thrust and lift. Of particular interest is to determine the effect of these oscillatory movements on the energetics of the swimmer.

(d) *Flexibility effects*. The current findings and hypotheses were derived based on rigid propulsors. It has been shown that flexible pitching panels produce thrust more efficiently than their rigid counterparts [79]. It is expected that adding flexibility to the current model will not change the current findings fundamentally but will improve thrust production which then translates into achieving higher speeds with the same input power (Power-speed line in Fig. 4.11b will be shifted downward). Of particular value will be to study the role of structural resonance in free-swimming.

(e) *Acceleration phase*. As a more general objective, it is of interest to model the acceleration phase of a given swimmer. Theoretically, it is possible to achieve a given cruising speed using an infinite number of flapping gaits. It is hypothesized that one particular gait allows the swimmer to reach steady state most efficiently while another gait corresponds to shortest duration of acceleration.

Bibliography

[1] Fish, F. E. Advantages of natural propulsive systems. *Marine Technology Society Journal 47,* 5 (2013), 47-44.

[2] Bandyopadhyay, P. R. Trends in biorobotic autonomous undersea vehicles, *IEEE Journal of Oceanic Engineering 30*, 1 (2005), 109–139.

[3] Lauder, G. V. and Tytell, E. D. Hydrodynamics of undulatory propulsion. *Fish Biomechanics 23* (2006).

[4] Barrett, D., Grosenbaugh, M., and Triantafyllou, M. The optimal control of a flexible hull robotic undersea vehicle propelled by an oscillating foil. *Proceedings of the Symposium on Autonomous Underwater Vehicle Technology, AUV'96*. (1996), 1–9.

[5] Yu, J., Tan, M., Wang, S., and Chen, E. Development of a biomimetic robotic fish and its control algorithm. Systems, Man and Cybernetics, Part B, *IEEE Transactions on 34*, 4 (2004), 1798–1810.

[6] Anderson, J. M., and Chhabra, N. K. Maneuvering and stability performance of a robotic tuna. *Integrative and Comparative Biology 42*, 1 (2002), 118–126.

[7] Ayers, J., Wilbur, C., and Olcott, C. Lamprey robots. *In The Interna-tional Symposium on Aqua-Biomechanisms* (2000).

[8] Crespi, A., Badertscher, A., Guignard, A., and Ijspeert, A. J. An amphibious robot capable of snake and lamprey-like locomotion. *Proceedings of 35th International Symposium of Robotics* (2004).

[9] Yu, J., Hu, Y., Fan, R., Wang, L., and Huo, J. Mechanical design and motion control of a biomimetic robotic dolphin. *Advanced Robotics 21*, 3 (2007), 499–513.

[10] Breder, C. M. The locomotion of fishes. *New York Zoological Society, New York* (1926).

[11] Lindsey C.C. Form, function and locomotory habits in fish. *Fish Physiology, Locomotion 7*, (1978) 1–100.

[12] Webb, P. W. The biology of fish swimming. Mechanics and Physiology of Animal Swimming (ed. L. Maddock, Q. Bone and J.M.V Rayner), Cambridge University Press, (1994), 45-62.

[13] Rosenberger, L. J. Pectoral fin locomotion in batoid fishes: undulation versus oscillation. *Journal of Experimental Biology 204*, (2001), 379-394.

[14] Walker, J. A. and Westneat, M. W. Mechanical performance of aquatic rowing and flying. *Proceeding of the Royal Scoiety B 267*, (2000), 1875-1881.

[15] Walker, J. A. and Westneat, M. W. Performance limits of labriform propulsion and correlates with fin shape and motion. *Journal of Experimental Biology 205*, (2002), 177-187.

[16] Clark, R. P., and Smits, A. J. Thrust production and wake structure of a batoid-inspired oscillating fin. *Journal of Fluid Mechanics 562* (2006), 415-429.

[17] Dewey, P. A., Boschitsch, B. M., Moored, K. W., Stone, H. A. and Smits, A. J. Scaling Triantafyllou laws for the thrust production of flexible pitching panels. *Journal of Fluid Mechanics 732*, 29 (2013).

[18] Moored, K. W. The design of a novel tensegrity-based synthetic pectoral fin for bio-inspired propulsion. PhD thesis, University of Virginia, 2010.

[19] Videler, J. J. and Weihs, D. Energetic advantages of burst-and-coast swimming of fish at high speeds. *Journal of Experimental Biology 97*, (1982), 169-178.

[20] Liao, J. C., Beal, D. N., Lauder, G. V. and Triantafyllou, M. S. Fish Exploiting Vortices Decrease Muscle Activity. *Science 302*, (2003), 1566-1569.

[21] Taylor, G. K., Nudds, R. L. and Thomas, A. L. R. Flying and swimming animals cruise at a Strouhal number tuned for high power efficiency. *Nature 425*, 707 (2003).

[22] Moored, K. W., Dewey, P. A., Leftwich, M. C., Bart-Smith, H. and Smits, A. J. Bioinspired propulsion mechanisms based on manta ray locomotion. *Marine Technology Society 45*, (2011), 110–118.

[23] Bainbridge, R. The speed of swimming of fish as related to size and to the frequency and amplitude of the tail beat. *Journal of Experimental Biology 35*, 109 (1958).

[24] Rohr, J. J. and Fish, F. E. Strouhal numbers and optimization of swimming by odontocete cetaceans. *Journal of Experimental Biology 207*, 1633 (2004).

[25] Heine, C. Mechanics of flapping fin locomotion in the cownose ray, rhinoptera bonasus (elasmobranchii: Myliobatidae). PhD thesis, Duke University, 1992.

[26] Knoller, R. Die Gesetze des Lufrwiderstandes. *Flug- und Motortechnik 3*, (1909), 1-7.

[27] Betz, A. Ein Beitrag zur Erkl¨arung des Segelfluges. *Z. Flugtech. Motorluftschiff. 3*, (1912), 269–272.

[28] Katzmayr, R. Effect of periodic changes of angle of attack on behavior of airfoils. Translation from "Zeitschrift fur Flugtechnik und Motorluftschiffahrt". *NACA TR TM 147*, (1922).

[29] Ober, S. Note on the Katzmayr effect on airfoil drag. *NACA TR TN 214*, (1925).

[30] Garrick, I. E. Propulsion of a flapping and oscillating airfoil. *NACA TR 567*, (1936).

[31] Glauert, H. The force and moment on an oscillating aerofoil. *Tech. Rep. Aero. Res. Comm. 1242*, (1929).

[32] Theodorsen, T. General theory of aerodynamic instability and the mechanism of flutter. *NACA TR 496*, (1935).

[33] Wang, Z. J. Vortex shedding and frequency selection in flapping flight. *Journal of Fluid Mechanics 410*, (2000), 323–341.

[34] Lighthill, M. J. Aquatic animal propulsion of high hydromechanical efficiency. *Journal of Fluid Mechanics 44*, (1970), 265–301.

[35] Chopra, M. G. and Kambe, T. Hydromechanics of lunate tail swimming propulsion. Part 2. *Journal of Fluid Mechanics 79*, (1977), 49–69.

[36] Chopra, M. G. Hydromechanics of lunate-tail swimming propulsion. *Journal of Fluid Mechanics 64*, (1974), 375–391.

[37] Wu, T. Y.-T. Hydromechanics of swimming propulsion. Part 1. Swimming of a two-dimensional flexible plate at variable forward speeds in an inviscid fluid. *Journal of Fluid Mechanics 46*, (1971), 337–355.

[38] Phlips, P. J., East, R. A. and Pratt, N. H. An unsteady lifting line theory of flapping wings with application to the forward flight of birds. *Journal of Fluid Mech*anics *112*, (1981), 97–125.

[39] Ahmadi, A. R. and Widnall, S. E. Energetics and optimum motion of oscillating lifting surfaces of finite span. *Journal of Fluid Mechanics 162*, (1986), 261–282.

[40] Willmott, P. Unsteady lifting-line theory by the method of matched asymptotic expansions. *Journal of Fluid Mechanics 186*, (1988), 303–320.

[41] Betteridge, D. J. and Archer, R. D. A study of the mechanics of flapping flight. *Aeronautical Quarterly 25*, (1974), 129–142.

[42] Archer, R. D., Sappupo, J. and Betteridge, D. J. Propulsive characteristics of flapping wings. *Aeronautical Journal 83*, (1979), 355–371.

[43] Hall, K. C. and Hall, S. R. Minimum induced power requirements for flapping flight. *Journal of Fluid Mechanics 323,* (1996), 285–315.

[44] Hall, K. C., Pigott, S. A. and Hall, S. R. Power requirements for large-amplitude flapping flight. *Journal of Aircraft 35*, (1998), 352–361.

[45] Katz, J. and Plotkin, A. Low-Speed Aerodynamics: From Wing Theory to Panel Methods. *McGraw-Hill*, (1991).

[46] Smith, M. J. C., Wilkin, P. J. and Williams, M. H. The advantages of an unsteady panel method in modeling the aerodynamic forces on rigid flapping wings. *Journal of Experimental Biology 199*, (1996), 1073–1083.

[47] Lewin, G. C., and Haj-Hariri, H. Modeling thrust generation of a two-dimensional heaving airfoil in a viscous flow. *Journal of Fluid Mechanics 492*, (2003).

[48] Jones, K. D., Dohring, C. M. and Platzer, M. F. Experimental and computational investigation of the Knoller–Betz effect. *AIAA Journal 37*, (1998), 1240–1246.

[49] Triantafyllou, M. S., Triantafyllou, G. S., and Gopalkrishnan, R. Wake Mechanics for Thrust Generation in Oscillating Foils. *Physics of Fluids A 3*, 2835 (1991).

[50] Triantafyllou, G. S., Triantafyllou, M. S. and Chryssostomidis, C. On the formation of vortex streets behind stationary cylinders. *Journal of Fluid Mechanics 170*, 461 (1986).

[51] Anderson, J. M., Streitlien, K., Barrett, D. S. and Truantafyllou, M. S. Oscillating foils of high propulsive efficiency. *Journal of Fluid Mechanics 360*, (1998), 41–72.

[52] Buchholz, J. H. J. and Smits, A. J. The wake structure and thrust performance of a rigid low-aspect-ratio pitching panel. *Journal of Fluid Mechanics 602*, (2008), 331–365.

[53] Godoy-Diana, R., Aider, J. L. and Wesfreid, J. E. Transitions in the wake of a flapping foil. *Physical Review E 77*, (2008).

[54] Lai, J. C. S. and Platzer, M. F. Jet characteristics of a plunging airfoil. *AIAA Journal 37*, (1999), 1529–1537.

[55] Schnipper, T., Andersen, A. and Bohr, T. Vortex wakes of a flapping foil. *Journal of Fluid Mechanics 633*, (2009), 411–423.

[56] Dong, H., Mital, R. and Najjar, F. M. Wake topology and hydrodynamic performance of low-aspect-ratio flapping foils. *Journal of Fluid Mechanics 566*, (2006), 309–343.

[57] Liu, H., Ellington, C. P., Kawachi, K., van den Berg, C. and Willmott, A. P. A computational fluid dynamics study of hawkmoth hovering. *Journal of Experimental Biology 201*, (1998), 461–477.

[58] Ellington, C. P., van den Berg, C., Willmott, A. P. and Thomas, A. L. R. Leading-edge vortices in insect flight. *Nature 384*, (1996), 626–630.

[59] Willmott, A. P. and Ellington, C. P. Measuring the angle of attack of beating insect wings: robust three-dimensional reconstruction from two-dimensional images. *Journal of Experimental Biology 200*, (1997a), 2693–2704.

[60] Willmott, A. P. and Ellington, C. P. The mechanics of flight in the hawkmoth manduca sexta I. Kinematics of hovering and forward flight. *Journal of Experimental Biology 200*, (1997b), 2705–2722.

[61] Koochesfahani, M. M. Vortical patterns in the wake of an oscillating airfoil. *AIAA Journal 27*, (1989), 1200–1205.

[62] Bohl, D. G. and Koochesfahani, M. M. MTV measurements of the vortical field in the wake of an airfoil oscillating at high reduced frequency. *Journal of Fluid Mechanics 620*, (2009), 63–88.

[63] Von Ellennrieder, K. D., Parker, K. and Soria, J. Flow structures behind a heaving and pitching finite-span wing. *Journal of Fluid Mechanics 490*, (2003), 129–138.

[64] Blondeaux, P., Fornarelli, F., Guglielmini, L., Triantafyllou, M. S. and Verzicco, R. Numerical experiments on flapping foils mimicking fish-like locomotion. *Physics of Fluids 17*, (2005).

[65] Dewey, P. A., Carriou, A. and Smits, A. J. On the relationship between efficiency and wake structure of a batoid-inspired oscillating fin. *Journal of Fluid Mechanics 691*, (2011), 245-266.

[66] Williamson, C. H. K. and Roshko, A. Vortex formation in the wake of an oscillating cylinder. *Journal of Fluids and Structure 2*, (1988), 355–381.

[67] Moored, K. W., Dewey, P. A., Smits, A. J. and Haj-Hariri, H. Hydrodynamic wake resonance as an underlying principle of efficient unsteady propulsion. *Journal of Fluid Mechanics 708*, (2012), 329-348.

[68] Triantafyllou, G. S., Triantafyllou, M. S. and Grosenbaugh, M. A. Optimal thrust development in oscillating foils with application to fish propulsion. *Journal of Fluids and structure 7*, (1993), 205–224.

[69] Pennycuick, C. J. Span-ratio analysis used to estimate effective lift:drag ratio in the double-crested cormorant Phalacrocorax auritus from field observations. *Journal of Experimental Biology 142*, (1989), 1–15.

[70] Rayner, Jeremy M. V. Mathematical modeling of the avian 2ight power curve. *Mathematical Methods in the Applied Sciences 24***,** (2001), 1485–1514.

[71] Schultz, W. W. and Webb, P. W. Power requirements of swimming: do new methods resolve old questions? *Integrative and Comparative Biology 42*, (2002), 1018-1025.

[72] Spedding, G.R. The aerodynamics of flight. *Advances in Comparative and Environmental Physiology 11, (*1992), 51.

[73] Borazjani, I. and Sotiropoulos, F. Numerical investigation of the hydrodynamics of carangiform swimming in the transitional and inertial flow regimes. *Journal of Experimental Biology 211*, (2008), 1541–1558.

[74] Webb, P. Bainbridge Sets The Stage On Scaling In Fish Swimming. *Journal of Experimental Biology 209*, (2006), 1789-1790.

[75] Russo, R. S. F. Biomechanical modeling of ray pectoral fins to inform the design of AUV propulsion systems. PhD thesis, University of Virginia, 2012.

[76] Menter, F. R. Zonal Two Equation k-ω Turbulence Models for Aerodynamic Flows. *AIAA Paper 93*, (1993), 2906.

[77] Green, M. A. and Smits, A. J. Effects of three-dimensionality on thrust production by a pitching panel. *Journal of Fluid Mechanics 615*, (2008), 211–220.

[78] Yano, K., Sato, F., and Takahashi, T. Observations of mating behavior of the manta ray, Manta birostris, at the Ogasawara Islands, Japan. *Ichthyological Research 46*, 3 (1999), 289–296.

[79] Quinn, D. B., Lauder, G. V., and Smits, A. J. Scaling the propulsive performance of heaving flexible panels. *Journal of Fluid Mechanics 738,* (2014), 250-267.

[80] Haj-Hariri, H. For free swimming the efficiency and economy optima are the same. American Physical Society, 64th Annual Meeting of the APS Division of Fluid Dynamics, abstract #G28.001, November 20-22, (2011).

[81] Kohannim, S. and Iwasaki, T. Analytical insights into optimality and resonance in fish swimming. *Journal of Royal Society Interface 11,* (2014).

[82] Wu T. Y. Fish Swimming and Bird/Insect Flight. *Annual Reviews of Fluid Mechanics 43*, (2011).

[83] Hoerner, S. F. Fluid Dynamics Drag. *Hoerner Fluid Dynamics*, *Bricktown New Jersey*, (1965).

[84] Webber, D. M., Boutilier, R. G., Kerr, S. R. and Smale, M. J. Caudal differential pressure as a predictor of swimming speed of cod (Gadus morhua). *Journal of Experimental Biology 204*, (2001), 3561-3570.

[85] ANSYS® Academic Research, Release 14.0, Help System, ANSYS CFX-Solver Theory Guide, ANSYS, Inc.

[86] Pauley, L. L., Moin, P. and Reynolds, W. C. The structure of two-dimensional separation. *Journal of Fluid Mechanics 220,* (1990), 397-412.

[87] Critzos, C. C., Heyson, H. H. and Boswinkle, R. W. Aerodynamic characteristics of NACA 0012 airfoil section at angles of attack from 0° to 180°. *NACA TN 3361,* (1955).

[88] McGhee, R. J., Walker, B. S. and Millard, B. F. Experimental results for the Eppler 387 airfoil at low Reynolds numbers in the Langley Low-Turbulence Pressure Tunnel. *NASA Technical Memorandum 4062*, (1988).

[89] Barth, T. J., and Jesperson, D. C. The Design and Application of Upwind Schemes on Unstructured Meshes. *AIAA Paper* 89-0366, (1989).

[90] Dewey, P. A. Private Communication, Jun 2013.

[91] Moored, K. W., Dewey, P. A., Boschitsch, B. A., Smits, A. J. and Haj-Hariri, H. Linear instability mechanisms leading to optimally efficient locomotion with flexible propulsors. *Physics of Fluids 26* , (2014).